



Title	Study on eukaryotic ribosome biogenesis
Author(s)	朝野, 希美
Citation	北海道大学. 博士(生命科学) 甲第11832号
Issue Date	2015-03-25
DOI	10.14943/doctoral.k11832
Doc URL	http://hdl.handle.net/2115/60992
Type	theses (doctoral)
File Information	Nozomi_Asano.pdf



[Instructions for use](#)

博士学位論文

Study on eukaryotic ribosome biogenesis

(真核生物リボソーム生合成についての研究)

北海道大学大学院生命科学院

生命科学専攻 生命融合科学コース

2015

朝野 希美

Contents

General Introduction.....	4
1 Ribosome.....	4
2 Overview of eukaryotic ribosome biogenesis.....	5
3 pre-rRNA processing scheme.....	6
Chapter I	8
Summary	8
1 Introduction	10
1.1 Recruitment of 5S rRNA, RpL5 and RpL11 to 90S.....	10
1.2 Assembling factors of ribosome biogenesis; Rpf2 and Rrs1	13
Chapter I-I	14
2 Material and methods	14
2.1 Plasmid construct.....	14
2.2 Protein co-expression and purification for crystallization	14
2.3 Crystallization and characterization of obtained crystals.....	15
2.4 Limited proteolysis analysis	16
2.5 Data collection and process for native crystal.....	17
2.6 Selenomethionine (SeMet)-labeled crystals for phase determination	18
3 Results and discussion.....	20
3.1 Protein expression and crystallization.....	20
3.2 Characterization of the obtained crystal	20
3.3 Domain composition of Rpf2 and Rrs1	22
3.4 Preliminary structure analysis	22
Chapter I-II.....	25
2 Material and methods	25
2.1 Plasmid construct, protein expression and purification for binding assay	25
2.3 <i>In vitro</i> rRNA transcription.....	26
2.5 Structure determination.....	28
2.6 Gel shift assays of Rpf2-Rrs1 mutants with 5S rRNA.....	29
2.7 Circular dichroism spectrum.....	29
3 Results	30
3.1 Overall structure	30
3.2 Detailed interaction between Rpf2 and Rrs1	32

3.3	5S rRNA binding assay for Rpf2- Rrs1 complex	37
3.4	Structural elements involved in binding between the Rpf2-Rrs1 complex and 5S rRNA	39
4	Discussion	43
4.1	Structural aspect of full-length Rpf2-Rrs1 complex	43
4.2	Rpf2/Brix domain as a highly evolutionarily modified scaffold domain.....	43
4.3	Role of Rrs1 and proline-rich linker	46
4.4	Binding model of Rpf2-subcomplex with 90S ribosome	48
 Chapter II.....		 50
Summary		50
1	Introduction	51
1.1	Final maturation step of pre-60S in cytoplasm	51
1.2	SBDS and EFL1	52
2	Material and methods	55
2.1	Plasmid construction	55
2.2	Protein expression and purification.....	57
2.3	Gel filtration analyses	57
2.5	Gel shift assay	58
2.6	Isothermal titration calorimetry.....	58
2.7	Circular dichroism measurements.....	58
2.8	Model building of EFL1-Tif6-bound ribosome	58
3	Results	59
3.1	Interaction between EFL1 and SBDS.....	59
3.2	Identification of the binding region in EFL1	61
3.3	Identification of the binding region in SBDS.....	64
4	Discussion	66
4.1	Biological implications of SBDS – EFL1 interaction.....	66
4.2	Role of the insertion domain of EFL1	68
 Reference.....		 69
 Acknowledgements.....		 73

General Introduction

1 Ribosome

Proteins are one kind of functional macromolecules that are essential for living cells. These molecules are synthesized by ribosomes which translate the genetic code in mRNA in all organisms. The ribosome is composed of two parts, called large and small subunits, which can dissociate and reunite. The bacterial 70S ribosome (named for its apparent sedimentation velocity) is made up of 50S and 30S subunits. On the other hand, the eukaryotic 80S ribosome is made up of 60S and 40S. Each of the subunits consists of some rRNAs and many ribosomal proteins. The eukaryotic ribosome is larger and more complex, which is composed of four ribosomal RNAs (25S, 18S, 5.8S, and 5S rRNAs) and approximately 80 ribosomal proteins. In 2010, the first crystal structure of the yeast 80S ribosome was reported (1). Subsequently, 80S structure with 3Å resolution was determined in 2011 (2). These structural analyses provide detailed molecular insights into the mechanisms of ribosome function. However, the biogenesis of eukaryotic ribosome remains unclear.

2 Overview of eukaryotic ribosome biogenesis

The construction of eukaryotic ribosome follows an ordered assembly of ribosomal proteins and four rRNAs into 60S and 40S ribosomal subunit. This process is spatially and temporally coordinated starting with co-transcriptional assembly of a first pre-ribosomal particle (90S) in the nucleolus. Then, 90S is subsequently separated into 60S precursor (pre-60S) and 40S precursor (pre-40S), which follow independent processing and maturation steps. These two ribosome precursors transit from the nucleolus through the nucleoplasm into the cytoplasm. After final maturation in cytoplasm, precursors form functional subunits (Fig. 1-1). Many processing steps in ribosome biogenesis have been elucidated by studies on *Saccharomyces cerevisiae*. More than 200 factors are required for these steps (3,4).

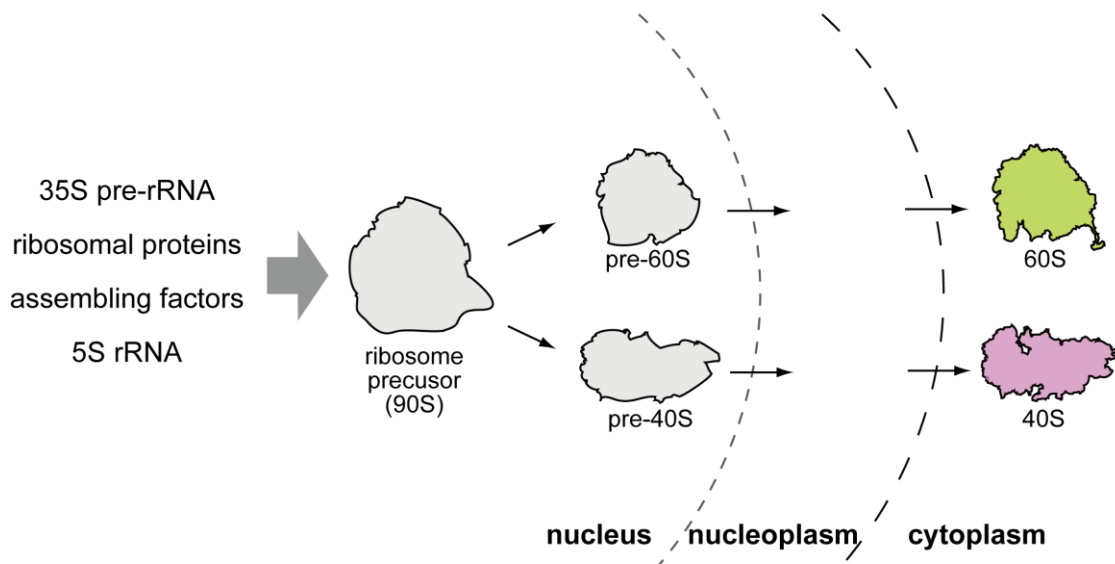


Fig. 1-1 Schematic view of eukaryotic ribosome biogenesis

3 pre-rRNA processing scheme

The biogenesis of this ribosome starts with the transcription of 35S pre-rRNA including 25S, 18S, and 5.8S rRNAs by RNA polymerase I and 5S rRNA by RNA polymerase III in the nucleolus. The pre-rRNA contains external and internal sequences that are not present in mature ribosomes. The extra sequences on 35S pre-rRNA are removed by the steps listed below to yield 27SA₂ and 20S pre-rRNAs. Depending on these steps, 90S is divided into two pre-ribosomal particles: pre-60S and pre-40S. The 5' cleavage of 27SA₂ generates 27SB, which is further divided into 7S and 25.5S (precursors of 5.8S and 25S rRNAs, respectively). After these processes, pre-60S and pre-40S transit to the cytoplasm to form mature functional subunits (5). On the other hand, 5S rRNA is only processed on its 3' terminal (Fig. 1-2). However it is unknown when the processing is occurred and 5S rRNA is recruited to 90S.

Processing of 27SB pre-rRNA is a control point in ribosome biogenesis; nascent ribosomes are released from the nucleolus into nucleoplasm once this step is completed (6). This step is believed to require major conformational rearrangements of pre-rRNPs (7,8). Fourteen assembling factors have been shown to be necessary for processing of 27SB pre-rRNA (9). Three of them are Rpf2, Rrs1 and Tif6.

In this study, I focus on two process of ribosome biogenesis related these three factors. One process is the recruitment of three ribosomal components (5S rRNA, Rpl5 and Rpl11) to 90S by Rpf2 and Rrs1 in upstream of ribosome biogenesis. The other process is removal of Tif6 from pre-60S by Efl1 and Sbd5 in final maturation at cytoplasm. I report the structural and functional analysis of Rpf2-Rrs1 complex in chapter I and the interaction analyses between Efl1 and Sbd5 in chapter II.

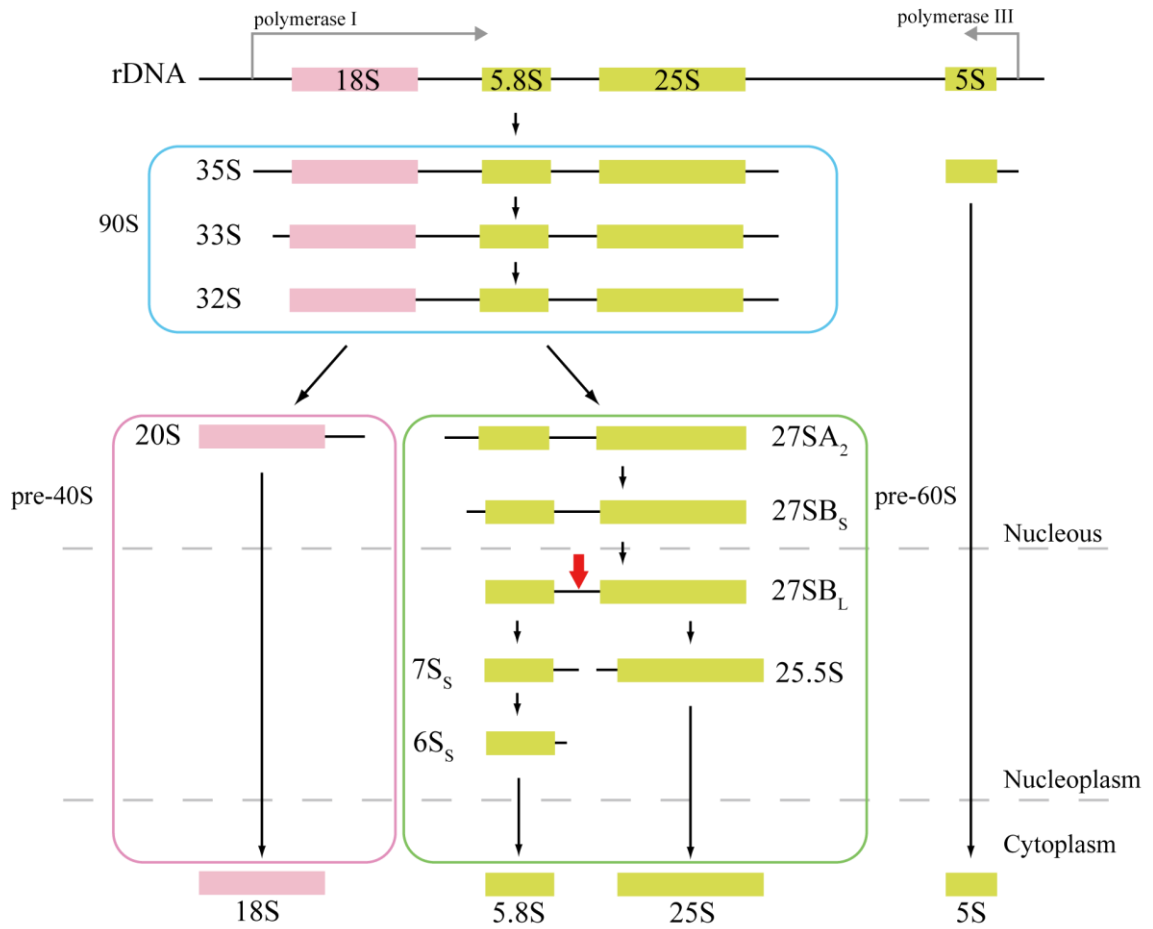


Fig. 1-2 pre-rRNA maturation pathway in *Saccharomyces cerevisiae*. Only major pathway is described. Red arrow shows cleaved site in 27SB processing.

Chapter I

Study on Rpf2-Rrs1 complex relating in recruitment of 5S rRNA, RpL5 and RpL11 to 90S ribosome precursor

Summary

Rpf2 and Rrs1 are essential proteins for ribosome biogenesis. These proteins are necessary for recruitment of three ribosomal components (5S rRNA, RpL5 and RpL11) to 90S ribosome precursor and subsequent processing of 27SB pre-rRNA. In 2007, Rpf2-subcomplex consisting of Rpf2, Rrs1, RpL5, RpL11 and 5S rRNA was isolated. Binding assays showed that these proteins were directly interacted. Among of them, the strong interaction between Rpf2 and Rrs1 suggested that Rpf2 and Rrs1 work as heterodimer. The detailed interactions are not clear. Furthermore, it is also unknown whether Rpf2 and Rrs1 directly associate with 5S rRNA.

In chapter I-I, I describe crystallization and preliminary X-ray crystallographic analysis of Rpf2-Rrs1. Rpf2 and Rrs1 from *Aspergillus nidulans* (*An*) were co-overexpressed in *Escherichia coli*, purified and crystallized. Subsequent analysis revealed that these crystals contained the central core region of the complex consisting of both N-terminal domains. X-ray diffraction data were collected to 2.35 Å resolution. Preliminary analysis revealed that the crystals belonged to space group $P2_12_12_1$, with unit-cell parameters $a = 54.1$, $b = 123.3$, $c = 133.8$ Å. There are two complexes in the asymmetric unit.

In chapter I-II, I present structural and functional analysis of Rpf2-Rrs1 complex. The core complex contains the tightly interlocked N-terminal domains of Rpf2 and Rrs1. The Rpf2 N-terminal domain includes a Brix domain characterized by similar N- and C-terminal architecture. The long α -helix of Rrs1 attend to the C-terminal half of the Brix domain as if it were part of a single molecule. The conserved proline-rich linker connecting the N- and C-terminal domains of Rrs1 wrap around the side of Rpf2 and anchor the C-terminal domain of Rrs1 to a specific site on Rpf2. In addition, gel shift analysis revealed that the Rpf2-Rrs1 complex binds directly to 5S rRNA. Further analysis of Rpf2-Rrs1 mutants demonstrated that *Saccharomyces cerevisiae* Rpf2 R236 (corresponds to R238 of *An*Rpf2) plays a significant role in this binding. Based on these studies and previous reports,

we have proposed a model for ribosomal component recruitment to the 90S ribosome precursor.

1 Introduction

1.1 Recruitment of 5S rRNA, RpL5 and RpL11 to 90S

In the first maturation step, unlike the other rRNAs (25S, 18S, 5.8S), the 5S rRNA is transcribed from separate linked genes by RNA polymerase III. The 5S rRNA is recruited to the 90S with two ribosomal proteins RpL5 and RpL11 by two assembling factors, Rpf2 and Rrs1 (Fig. 1-3). This recruitment is necessary for 90S and pre-60S maturation.

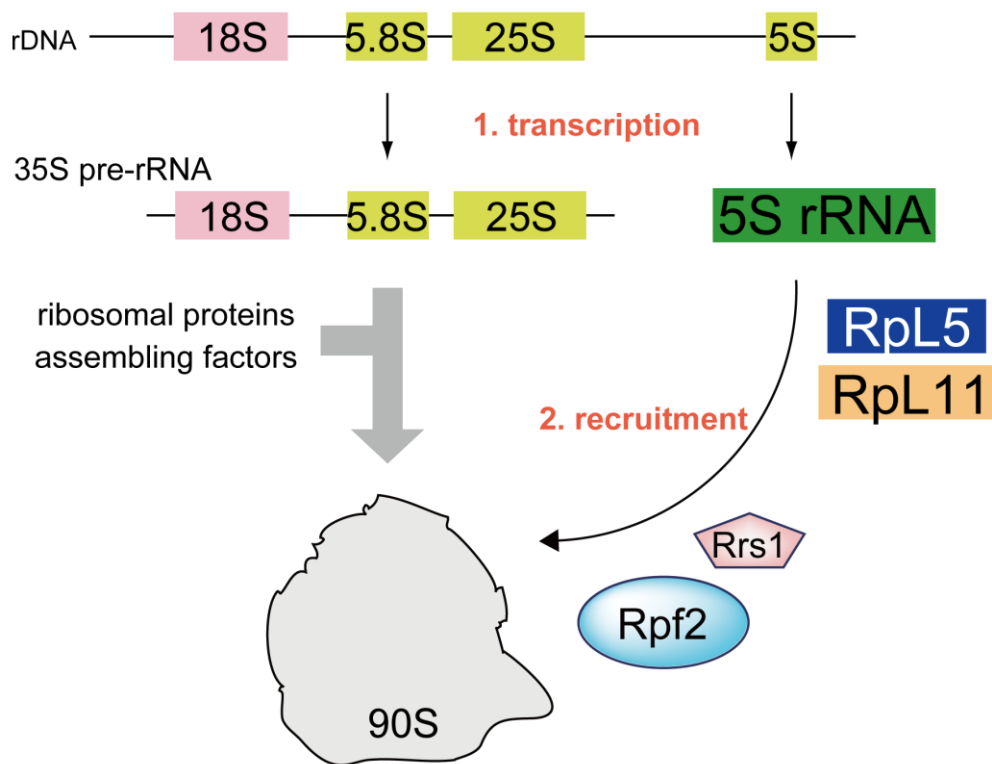


Fig. 1-3 Recruitment of 5S rRNA, RpL5 and RpL11 to 90S ribosome precursor

In 2007, an Rpf2-subcomplex comprising two assembly factors (Rpf2 and Rrs1), two ribosomal proteins (RpL5 and RpL11) and 5S rRNA was isolated from *Saccharomyces cerevisiae* (*Sc*) (10). These factors assembled into a 90S precursor containing 35S pre-rRNA (10). Genetic depletion of each of the four proteins inhibited the recruitment of the other three proteins and 5S rRNA to the 90S precursor (10). Moreover, depletion blocked the conversion of 27SB pre-rRNA to 7S and 25.5S pre-rRNA (11,12). These results suggested that Rpf2 and Rrs1 load 5S rRNA, RpL5 and RpL11 into the 90S precursor (Fig. 1-4). 27SB pre-rRNA processing occurs subsequent to this recruitment, indicating that the correct recruitment of 5S rRNA, RpL5, RpL11, Rpf2 and Rrs1 is a checkpoint of ribosome biogenesis. Yeast two-hybrid assays and GST pull-down experiments revealed direct interactions between these proteins (10,12-15) (Fig. 1-5). Among these interactions, the strong interaction between Rpf2 and Rrs1 suggested that these proteins function as a heterodimer. Although L65 in *Sc*Rrs1 is known to be critical for interactions of Rrs1 with RpL5 and RpL11 (15), details of the other interactions are not clear. Furthermore, it is also unknown whether the Rpf2-Rrs1 complex directly associates with 5S rRNA.

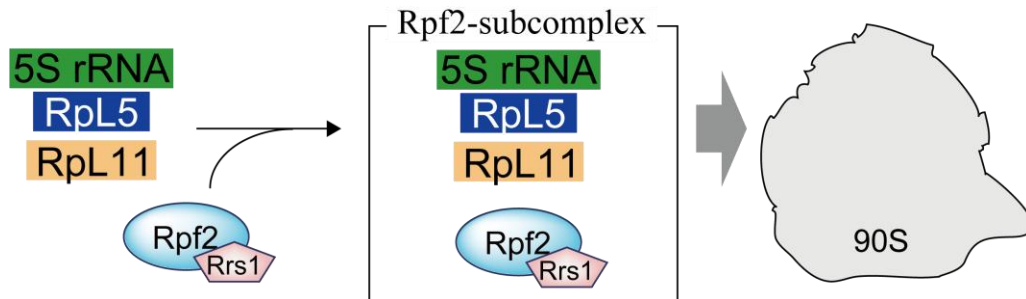


Fig. 1-4 Recruitment pathway of 5S rRNA to 90S

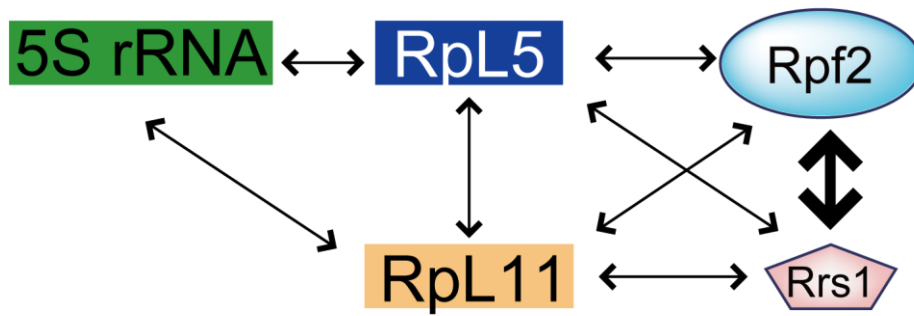


Fig. 1-5 Correlation diagram of direct interaction among Rpf2-subcomplex.

1.2 Assembling factors of ribosome biogenesis; Rpf2 and Rrs1

Rpf2 is an Imp4 superfamily protein. Although proteins in this family play distinct roles at different stages of ribosome biogenesis, all have a similar domain architecture consisting of a central globular Brix domain and optional highly charged N- and C-terminal segments (16). The Brix domain consists of a short peptide that is highly related to both a DNA-binding motif in the *E. coli* σ^{70} transcription factor and a eukaryotic RNA-binding domain (11). Brix domain function was characterized in a study of Imp4. The Imp4/Brix domain can associate with U3 small nucleolar RNA (snoRNA) and Mpp10, which is required for 35S pre-rRNA processing, to release 18S pre-rRNA for initiating small subunit biogenesis by itself (17,18). Moreover, single-stranded telomeric DNA has been reported to bind to the Imp4/Brix domain (19). A structural analysis of the Imp4-like protein Mil revealed the characteristic architecture of the Brix domain, which features a similar arrangement of structural elements in its N- and C-terminal halves (20). Although the Brix domain serves as a scaffold for interactions with several binding partners, these interactions are not well understood.

Rrs1 was isolated as a factor related to a secretory defect that caused the transcriptional repression of both rRNA and ribosomal protein genes (21). This protein was known to localize to the nucleolus and nuclear periphery. In the nucleolus, Rrs1 acts as a ribosome assembly factor. At the nuclear periphery, it directly interacts with the membrane-spanning SUN domain protein Mps3 and silent information factor Sir4, which are involved in telomere clustering and silencing (22).

To shed light on ribosome biogenesis from a structural point of view, I began to elucidate the structures of Rpf2 and Rrs1 proteins. This thesis is organized into two sections. In Chapter I, crystallization and preliminary X-ray crystallographic analysis is described. In Chapter II, the crystal structure of Rpf2-Rrs1 N-terminal domain complex and binding of 5S rRNA are described.

Chapter I-I

Crystallization and preliminary X-ray crystallographic analysis

2 Material and methods

2.1 Plasmid construct

The gene containing the coding region for a C-terminal truncated form (delta 305–332) of *Aspergillus nidulans* (*An*) Rpf2 (residues 1–304) was cloned between the NdeI and XhoI sites of the expression plasmid pET28a (Novagen), modified by the addition of D-box fused with an N-terminal His 6 tag (cleavable by TEV protease). The gene encoding *AnRrs1* was cloned between the NdeI and NcoI sites of the expression plasmid pCDF Duet1 (Novagen), modified by the addition of D-box.

2.2 Protein co-expression and purification for crystallization

E. coli B834 (DE3) pRARE2 was transformed with pET28a–Rpf2(1–304) and pCDF Duet1–Rrs1, and the obtained colonies were tested for co-expression of both subunits. Cells were grown at 310 K in LB medium in the presence of 25 µg/ml kanamycin, 50 µg/ml streptomycin, and 34 µg/ml chloramphenicol to an OD₆₀₀ of 0.6. The culture was then induced by the addition of isopropyl β-D-1-thiogalactopyranoside (IPTG) to a final concentration of 0.25 mM and shifted to 298 K. After 16 h of incubation with constant shaking, the cells were harvested by centrifugation at 4500 g for 30 min at 277 K; washed with a solution containing 50 mM Tris–HCl pH 7.5, 300 mM NaCl, and 10% glycerol; and stored at 203 K until use.

The cell pellets (from 3 L culture) were resuspended in suspension buffer (50 mM Tris–HCl pH 7.5, 600 mM NaCl, and 10% (v/v) glycerol) added with 0.1 mg/ml DNase, 0.5 mg/ml lysozyme, and a protease inhibitor cocktail (complete EDTA-free; Roche) and were disrupted by sonication. The lysate was centrifuged for 30 min at 40000 g and 277 K. The supernatant was collected and filtered through 0.22-µm-pore-size filters (Sterivex; Millipore).

The supernatant was loaded onto a HisTrap HP column (GE Healthcare) preequilibrated with suspension buffer using an AKTA purifier system (GE Healthcare). Then, the column was subsequently washed with 4 % solution of the elution buffer (50 mM Tris–HCl pH 7.5, 600 mM NaCl, 10% (v/v) glycerol, and 500 mM imidazole) The protein was eluted with 50% elution buffer. The fractions containing the *AnRpf2*(1–304)–

Rrs1 complex were pooled and diluted up to 3-fold with dilution buffer (50 mM Tris–HCl pH 7.5 containing 5% (v/v) glycerol). The sample was further purified using a Resource S column (GE Healthcare) equilibrated with the dilution buffer. The complex was eluted with a linear gradient of 0.2–2 M sodium chloride in the same buffer. Fractions containing the target complex were subsequently loaded onto a HiLoad 16/60 Superdex 200 prep-grade column (GE Healthcare) equilibrated with SEC buffer (20 mM HEPES–NaOH buffer pH 7.5, 50 mM NaCl, and 1% (v/v) glycerol) and eluted with the same buffer. The peak fractions were concentrated and stored at 190 K. The purity of the complex was assessed by SDS-PAGE (Fig. 1-8(a)). In total, 4.2 mg of the purified *AnRpf2(1-304)*–Rrs1 complex was obtained from 3 L culture. All purification steps were performed at 277 K or on ice.

2.3 Crystallization and characterization of obtained crystals

Prior to crystallization trials, the purified complex was concentrated to 14 mg/ml in SEC buffer using a Millipore centrifugal filter device (Amicon Ultra-4, 10-kDa cutoff; Millipore). Crystallization screening was performed using JCSG Core I–IV Suites and Classics Suite (Qiagen) using the sitting-drop vapor-diffusion method in 96-well plates (NeXtal Evolution μ plate; Qiagen) with additive reagent of CPAPhS (23). Drops were formed by mixing 0.75 μ l of protein solution, 0.75 μ l of SEC buffer containing 45 ng/ μ l CPAPhS, and 0.75 μ l of reservoir solution and were equilibrated against 0.75 ml of reservoir solution at 293 K. Crystals were grown from JCSG Core I condition No. 34 (0.1 M HEPES–NaOH pH 6.5, 20% (w/v) PEG 6000 (final pH 7.0); Fig. 2). Isolated crystals were dissolved and analyzed by SDS-PAGE and matrix-assisted laser desorption ionization time-of-flight mass spectrometry (MALDI-TOF MS). These results showed that the crystal had two fragments (about 30 and 10 kDa fragments). To identify the two fragments, the 30-kDa band of SDS-PAGE was transferred onto a polyvinylidene difluoride (PVDF) membrane and sequenced using automatic Edman degradation.

2.4 Limited proteolysis analysis

For further identification of the crystallized components, I performed limited proteolysis by trypsin. Following Ni-affinity chromatography, a pooled fraction of the *AnRpf2del-Rrs1* complex was incubated with trypsin (Sigma) at a w/w ratio of 100:1 (*AnRpf2del-Rrs1*:trypsin) in buffer containing 50 mM Tris-HCl pH 7.5, 350 mM NaCl, 100 mM imidazole, and 7% (v/v) glycerol at 277 K for 1 h. To separate trypsin and cleavage products, the mixture was further purified using a Hitrap Heparin column (GE Healthcare) equilibrated with the dilution buffer. Protein was eluted with a linear gradient of 0.2–1 M sodium chloride in the same dilution buffer. Fractions containing the target protein were then loaded onto a HiLoad 16/60 Superdex 200 prep-grade column equilibrated with the above-mentioned SEC buffer. The purified digestion mixtures were analyzed by SDS-PAGE. The gel was stained with Coomassie blue. The N-terminal sequence of the product at the 10-kDa band was determined using the above-mentioned method.

2.5 Data collection and process for native crystal

X-ray diffraction data of this complex crystal were collected on beamline BL41XU of the SPring-8 (Harima, Japan) using a Rayonix MX225HE detector (proposal No. 2012A1494). Prior to the experiment, the crystals were cryoprotected by transfer into a solution containing 20% (v/v) glycerol for a few seconds and flash-cooled. In total, 720 images were collected with 0.5 oscillation and 1 s exposure time per image. The entire diffraction data set were indexed, integrated, merged, and scaled using XDS (24). The crystal diffracted to 2.35 Å resolution (Fig. 1-6) and belonged to space group $P2_12_12_1$, with unit-cell parameters ($a = 54.1$, $b = 123.3$, $c = 133.8$ Å). Matthews coefficient (25) suggested that two complexes were present in the asymmetric unit. Details of the data collection and processing statistics are provided in Table 1-1.

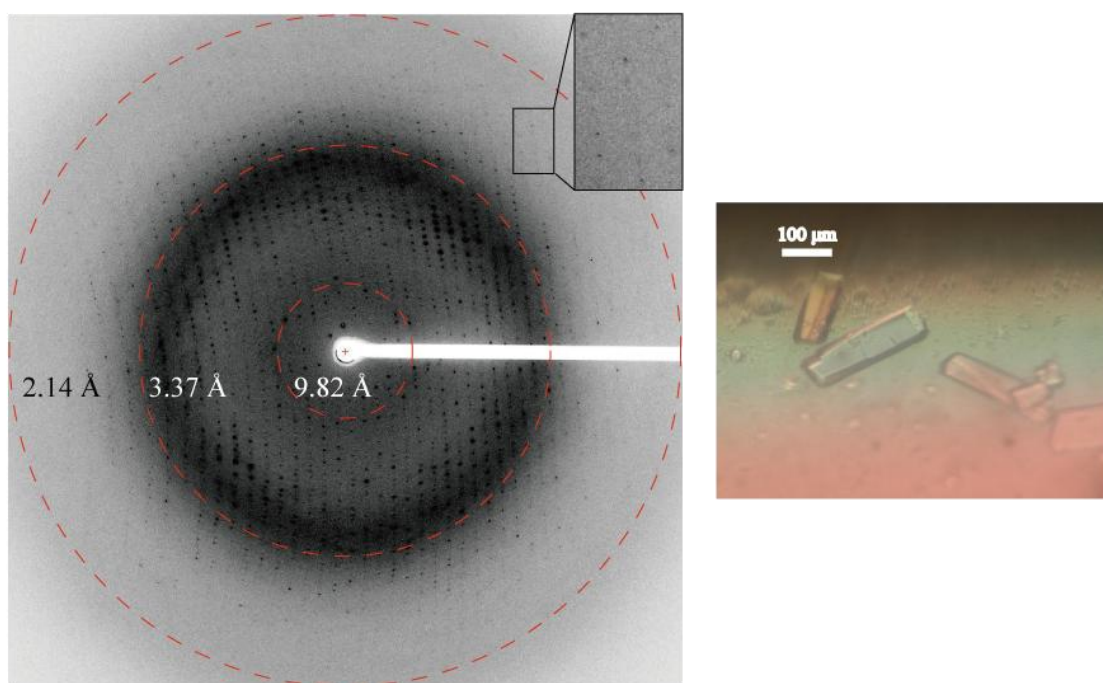


Fig. 1-6 (left) X-ray diffraction pattern of Rpf2-Rrs1 complex of native crystal. (right) Native crystals of Rpf2-Rrs1 complex

2.6 Selenomethionine (SeMet)-labeled crystals for phase determination

For phasing by anomalous dispersion using the selenium edge, I also produced SeMet-labeled Rpf2(18–254)–Rrs1(10–114) crystals. The optimized crystallization condition was 0.1 M HEPES–NaOH pH8.0, 14% (w/v) PEG 3350 and 300 mM NaCl (Fig. 1-7). The SeMet-labeled Rpf2(18–254)–Rrs1(10–114) crystals were cryoprotected with 20% (v/v) glycerol. The single-wavelength anomalous diffraction (SAD) data set was collected at PF AR-NE3A (Tsukuba, Japan) using an ADSC Quantum 270 CCD detector at a wavelength of 0.9788 Å. The wavelength for the collection of Se-SAD data was chosen on the basis of the fluorescence spectrum of the Se K absorption edge (Rice et al., 2000). The crystal belonged to space group $P4_12_12$, with unit-cell parameters ($a = b = 128.9$, $c = 57.5$ Å), and diffracted to 3.5 Å resolution. Details of the data collection and processing statistics are provided in Table 1-1. Phase calculation, density modification, and preliminary model building were performed using PHENIX AutoSol (26). All selenium sites of 10 were found and used for phasing.

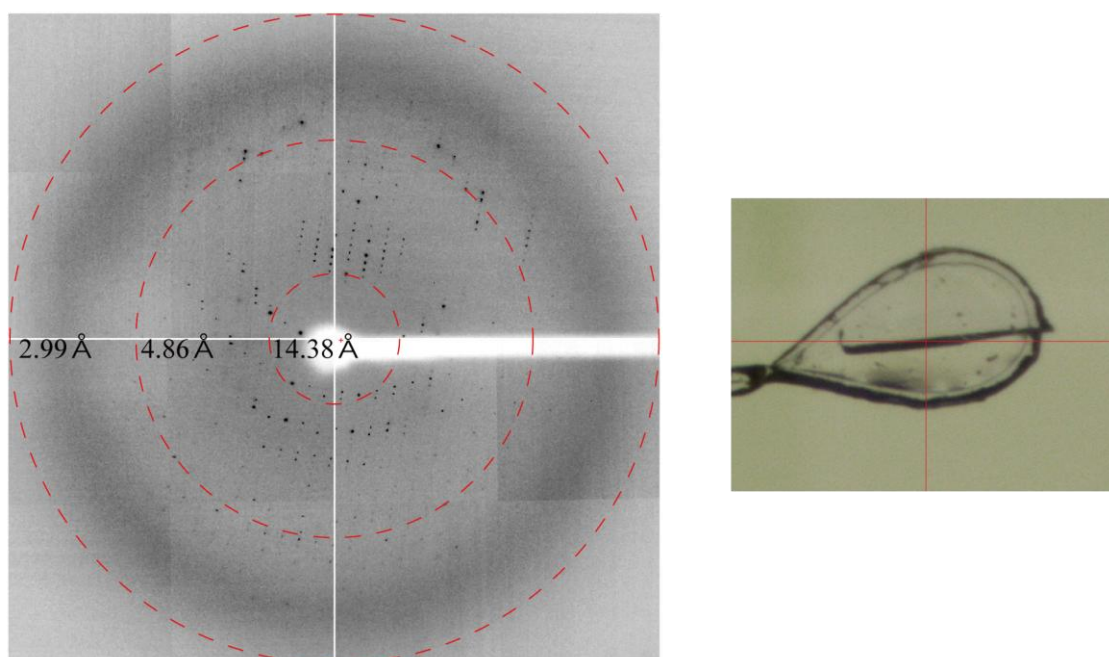


Fig. 1-7 (left) X-ray diffraction pattern of Rpf2-Rrs1 complex of Se-Met crystal. (right) Se-Met crystals of Rpf2-Rrs1 complex

Table 1-1

Statistics of data collection

Values in parentheses are for the highest resolution shell.

	Native crystal	SeMet-labeled crystal
Diffraction source	BL41XU, SPring-8	NE-3A, Photon factory
Wavelength (Å)	1.0000	0.9788
Temperature (K)	100	100
Detector	Rayonix MX225HE	ADSC Quantum 270 CCD
Crystal-detector distance (mm)	220	397.1
Rotation range per image (°)	0.5	0.8
Total rotation range (°)	180	180
Exposure time per image (s)	1	1.5
Space group	$P2_12_12_1$	$P4_12_12$
a, b, c (Å)	54.1, 123.3, 133.8	128.9, 128.9, 57.5
α, β, γ (°)	90, 90, 90	90, 90, 90
Mosaicity (°)	0.152	0.219
Resolution range (Å)	50 - 2.35 (2.49 - 2.35)	50-3.51(3.71-3.51)
Total No. of reflections	274543 (43024)	87626 (13867)
No. of unique reflections	38131 (5930)	11215 (1781)
Completeness (%)	99.4 (97.6)	99.9 (99.7)
Multiplicity	7.20 (7.26)	7.81 (7.56)
$\langle I/\sigma(I) \rangle$	14.51 (2.57)	12.96 (1.95)
R_{meas}	9.1 (77.6)	15.7 (108.3)
Overall B factor from Wilson plot (Å ²)	56.8	89.5

[†] $R_{meas} = \sqrt{\sum_{hkl} \{N(hkl)/[N(hkl) - 1]\}^{1/2} \sum_i |I_i(hkl) - \langle I(hkl) \rangle| / \sum_{hkl} \sum_i I_i(hkl)}$, where $\langle I(hkl) \rangle$ and $N(hkl)$ are the mean intensity of a set of equivalent reflections and the multiplicity, respectively.

3 Results and discussion

3.1 Protein expression and crystallization

Our first attempt to purify full-length Rrs1 from *S. cerevisiae* (ScRrs1: 1–218) was unsuccessful because it precipitated during purification. In addition, full-length ScRpf2 (1–322) was not expressed in *E. coli*. Because the interaction between Rrs1 and Rpf2 is strong (10,12), I reasoned that these proteins would form a stable complex. Therefore, I co-expressed Rpf2 and Rrs1 in *E. coli* and successfully purified them as a complex. However, Rpf2 in the complex was prone to be degraded. The results of western blotting using an N-terminal His 6 tag fused to Rpf2 and a disorder prediction program suggested that the C-terminal region of Rpf2 is degraded. Therefore, I constructed C-terminal deletion variants, the nonconserved region of which is deleted. I tried to prepare and perform crystallization screening using homolog proteins from several different species (*Saccharomyces cerevisiae*, *Candida albicans*, *Chaetomium thermophilum* and *Aspergillus nidulans*) and finally obtained crystals of the Rpf2–Rrs1 complex from *A. nidulans*.

3.2 Characterization of the obtained crystal

SDS-PAGE analysis of dissolved crystals suggested the presence of a single species at around 30 kDa and 10 kDa which are not intact proteins (Fig. 1-8(b)). In addition, the dissolved crystals were analyzed by MALDI-TOF MS. The mass-spectrometric results revealed that the crystals had a mass of 27342 Da and 11334 Da (Fig. 1-9). The sequence of the 20 N-terminal amino-acid residues of the 30-kDa fragment was determined to be ¹⁸AKEPQLIEGAKRVLLHGSK³⁷ from *AnRpf2*, suggesting that the crystals contained degraded *AnRpf2*. On the other hand, the 10-kDa band could not be identified because the amount of the applied crystals was too small.

Limited proteolysis by trypsin showed that single species were present at around 30 kDa and 10 kDa, suggesting that the composition of the trypsin-treated sample was similar to that of the obtained crystals (Fig. 1-8(c)). The sequence of the eight N-terminal amino-acid residues was determined to be ¹⁰STIKPKPE¹⁷ from *AnRrs1*.

Taken together, molecular-weight determination using mass spectrometry and N-terminal amino-acid sequencing revealed that the crystallized components are the N-terminal domains of *AnRpf2* (residues 18–262) and *AnRrs1* (residues 10–113), and that the remaining C-terminal regions were degraded during the crystallization process.

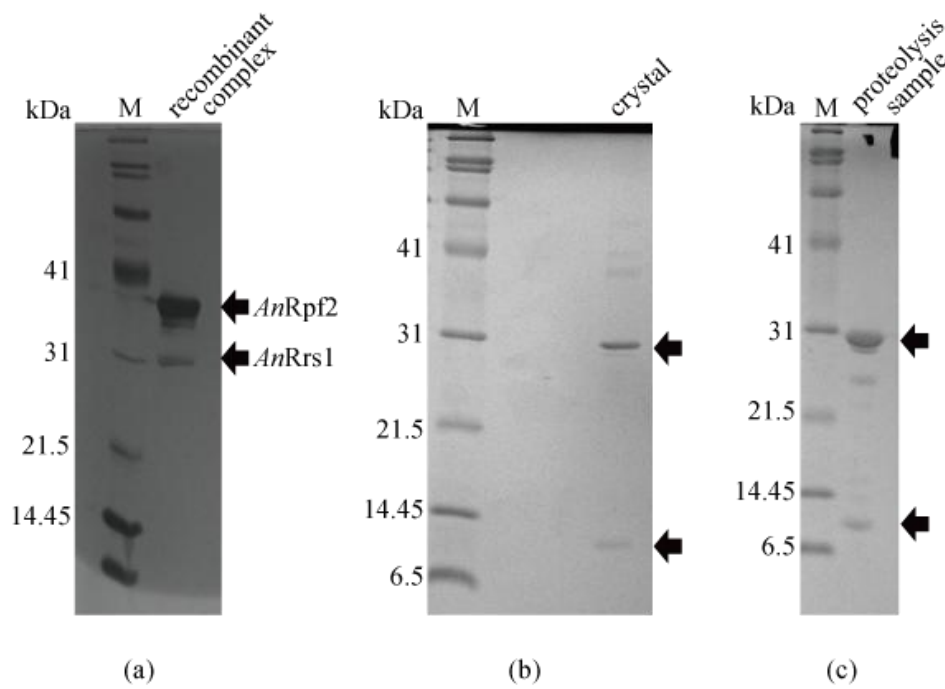


Fig. 1-8 15% SDS-PAGE gel stained by Coomassie Brilliant Blue. (a) Recombinant *An Rpf2*–*Rrs1* produced in *E.coli* after purification. (b) Crystal. (c) Cleavage products by trypsin. Lane M contains molecular-mass marker (labeled in kDa).

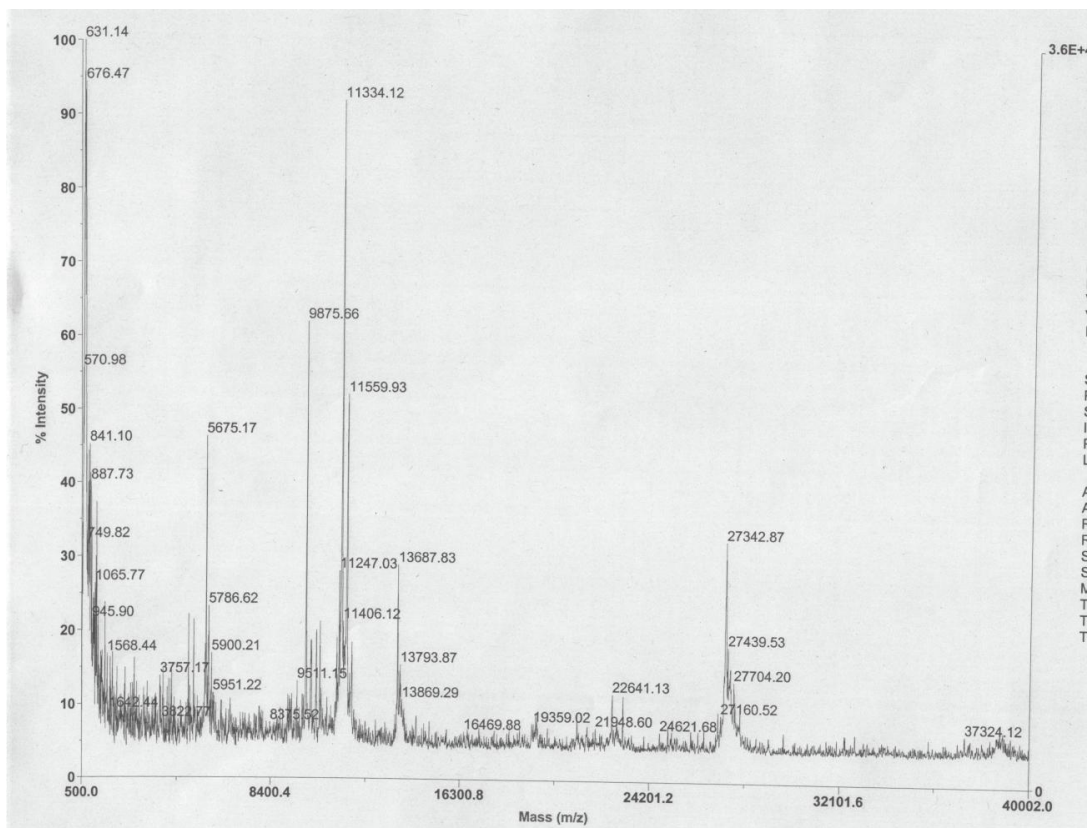


Fig. 1-9 MALDI-TOF Mass Spectra of the obtained crystal. Molecular mass of the components of the crystal was determined.

3.3 Domain composition of Rpf2 and Rrs1

Consistent with above mentioned results, PSIPRED and DISOPRED2 programs for predicting the secondary structure and the disorder region, respectively (27,28) (Fig. 1-10, 1-11, 1-12), suggested that residues 250–270 and C-terminal region (290–304) of *An*Rpf2 are disordered. In addition, secondary structure prediction of Rrs1 suggested that it has N- and C-terminal domains connected by the central linker region (residues 88–108), implying that these N- and C-terminal regions might behave separately. Furthermore, I examined the limited proteolysis of the free Rpf2 molecule and found that the N-terminal domain is also fragmented (data not shown). These results indicate that the tight core region of the Rpf2–Rrs1 complex is crystallized after scission of the remaining residues not involved in the interactions. Such highly flexible terminal domains of both proteins may prevent the production of full-length complex crystal.

3.4 Preliminary structure analysis

Preliminary structure analysis revealed that the native crystal contains two Rpf2–Rrs1 complexes in an asymmetric unit with a solvent content of 57%. On the other hand, the SeMet-labeled crystal contains one complex in an asymmetric unit with a solvent content of 58%.

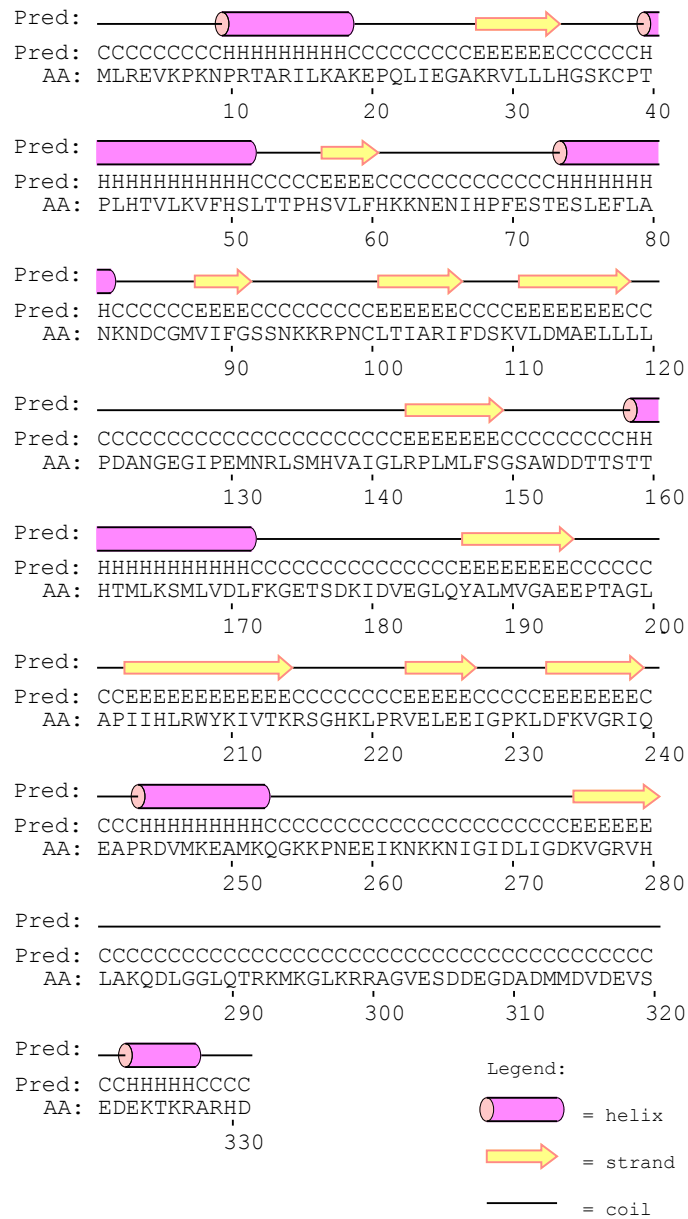


Fig. 1-10 Prediction of secondary structure of *AnRpf2*. Pred; predicted secondary structure, AA; target sequence.

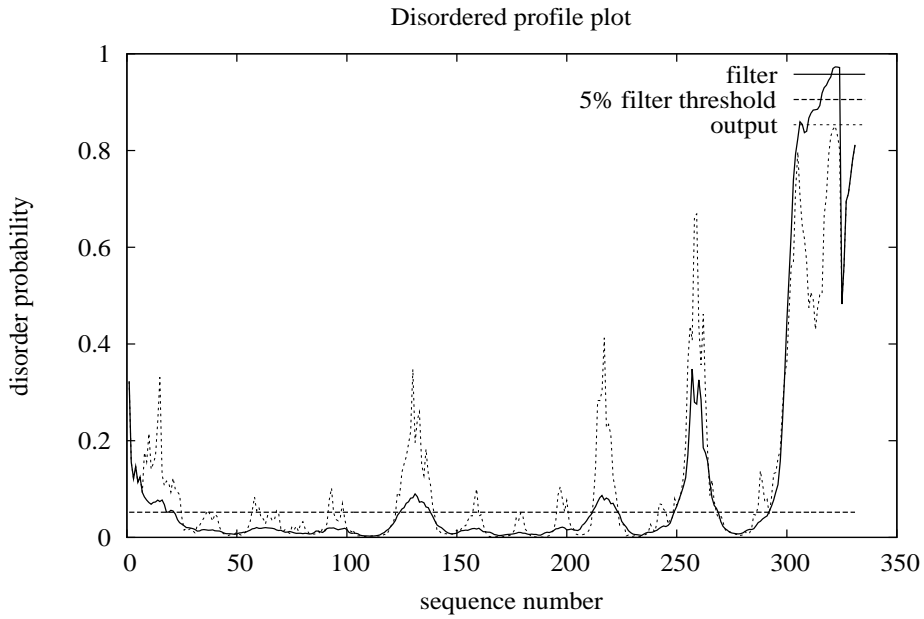


Fig. 1-11 Prediction of disorder region in *AnRpf2*

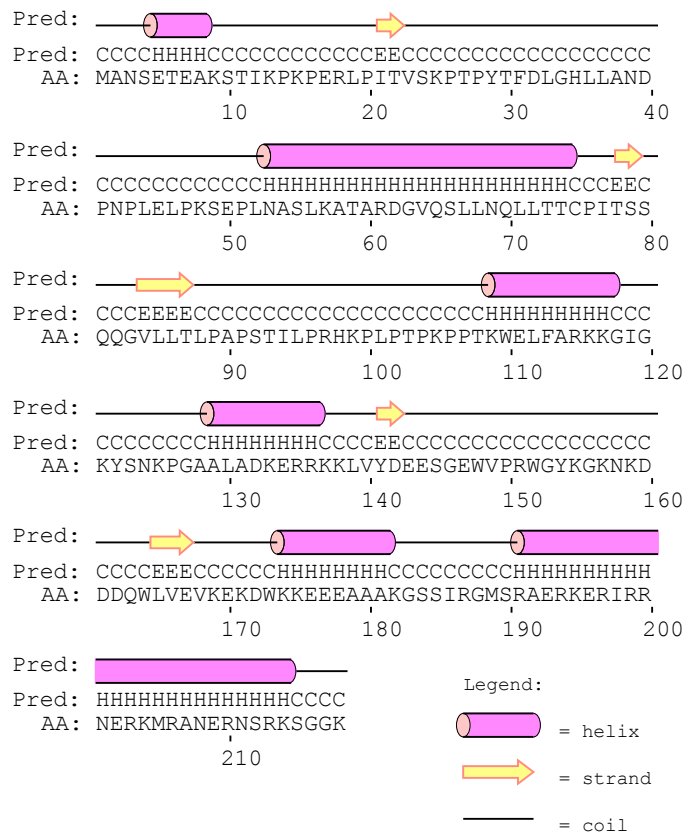


Fig. 1-12 Prediction of secondary structure of *AnRrs1*. Pred; predicted secondary structure, AA; target sequence.

Chapter I-II

Structural and functional analysis of Rpf2-Rrs1 complex

2 Material and methods

2.1 Plasmid construct, protein expression and purification for binding assay

The coding sequences for *ScRpf2* were amplified by PCR and inserted into pET28a (Novagen) modified by the addition of D-box fused with an N-terminal His 6 tag (cleavable by TEV protease). The plasmids for *ScRpf2* C-terminal deletion mutant (*ScRpf2* Δ C; deletion of 90 C-terminal residues, 255–344 aa) and point mutation variants were constructed by the inverse PCR method. Details of the templates and primers used in this study are described in the Table 1-2 and 1-3.

The coding sequences for *ScRrs1* were amplified by PCR and inserted into pCDF Duet1 (Novagen) that was modified by the addition of D-box. The plasmid for the *ScRrs1* C-terminal deletion mutant (*ScRrs1* Δ C; deletion of 94 C-terminal residues, 110–293 aa) was constructed using an inverse PCR method with the *ScRrs1* expression vector as a template. All vectors were confirmed by plasmid DNA sequencing.

The expressed *ScRpf2*-*Rrs1* full-length complex was purified using a previously described method (29). Instead of a Resource S column, we used a HisTrap heparin column (GE Healthcare) and performed size-exclusion chromatography with a different SEC buffer (20 mM HEPES-NaOH pH 7.5, 300 mM NaCl, 10 mM MgCl₂ and 10% (v/v) glycerol). Three C-terminal deletion complexes (*ScRpf2* Δ C-*Rrs1*, *ScRpf2*-*Rrs1* Δ C, *ScRpf2* Δ C-*Rrs1* Δ C) were prepared using the same method.

The point-mutated *ScRpf2* variants and *ScRpf2* Δ C were co-expressed with *ScRrs1* Δ C. The expressed complexes were purified on a HisTrap HP column and HiLoad 16/60 Superdex 200-pg column, followed by dialysis against dialysis buffer (20 mM HEPES-NaOH pH 7.5, 300 mM NaCl, 10 mM MgCl₂, 1 mM DTT, 50% (v/v) glycerol); the purified products were stored at -30°C.

2.3 *In vitro* rRNA transcription

Sc5S rRNA was prepared via *in vitro* transcription using T7 RNA polymerase. The DNA oligonucleotides used to construct *Sc5S* rDNA are described in Table 1-3. The 5S_S1~6 and 5S_AS1~6 primers were mixed and annealed after heating at 90°C for 5 min, followed by a subsequent cool down to 4°C at 0.1°C /12 sec. The fragment was cloned into pUC19 via the EcoRI and HindIII sites. The 5S rDNA sequence was confirmed by plasmid DNA sequencing. Double-strand DNA transcription templates were obtained via PCR with 5S_S-1 and 5S_AS-7. *In vitro* transcription was performed overnight at 37°C in a solution containing 80 mM HEPES-NaOH pH 8.1, 20 mM MgCl₂, 2.04 mM spermine, 20 mM DTT, 40 mM KCl, 1.4 µg/ml BSA, 5 mM NTPs, 20 mM GMP, 2.5 µg/ml transcription template, 0.1 U/ml pyrophosphatase and 0.24 mg/ml T7 RNA polymerase. The reaction mixture was subsequently isopropanol-precipitated, purified by denaturing urea-polyacrylamide gel electrophoresis and extracted with an Elutrap Electroelution system (Whatman plc). Pooled 5S rRNAs were precipitated with ethanol and resuspended in RNA buffer (20 mM Tris-HCl pH 7.5, 300 mM NaCl, 10 mM MgCl₂, 10% (v/v) glycerol).

Table 1-2 Summary of mutant construction

Mutant No.	Template	Primer	Mutation	Mutated region name
1	<i>ScRpf2</i> ΔC	S1, AS1	K62A, K63A	region-1
2	<i>ScRpf2</i> ΔC	S2, AS2	K81A	region-2
3	<i>ScRpf2</i> ΔC	S3, AS3	K94A, K95A, R96A	region-3
4	<i>ScRpf2</i> ΔC	S4, AS4	R236A	region-4
5	mutant 3	S4, AS4	K94A, K95A, R96A, R236A	
6	mutant 1	S3, AS3	K62A, K63A, K94A, K95A, R96A	
7	mutant 1	S4, AS4	K62A, K63A, R236A	
8	mutant 5	S1, AS1	K62A, K63A, K94A, K95A, R96A, R236A	
9	<i>ScRpf2</i> ΔC	S5, AS5	P68A, F69A, E70A	region-5

Table 1-3 Primer used in this study

Primer No.	Sequence
S1	AATgcggcgAATGATATTCATCCTTTCGAAGACATGTC
S2	GAAgcgAATGACTGTTCAATTGATGGTGCTGATG
S3	TCCgcggcgAAACAACATGACCTTTATACGTACATTTG
S4	GGCgcgATTCATACTCCAAGTCCAGATATGGTCACT
S5	CATgcggcgGACATGTCGCCACTAGAGTTCTTTAGTG
5S_S-1	AATTCTAAT ACGACTCACT TATAGGTTGCGGCCATATCTACCAGAAA
5S_S-2	GCACCGTTTCCCGTCCGATCAACTGTAGTTAAGCTGGTAAGAGCCTGACC
5S_S-3	GAGTAGTGTAGTGGGTGACCATACGCGAAACTCAGGTGCTGCAGT CGACG
5S_S-4	<i>GAGTCTAGACTCCGTCCTGATGAGTCCGTG</i>
5S_S-5	<i>AGGACGAAACTGCAAATAAACCAAGGATCAA</i>
5S_S-6	CCCCTTGGGGCCTCTAAACGGGTCTTGAGGGGTTTTTTGA
AS1	GAACCTCTTCATATCTGGCTTCTTCAAG
AS2	ACTAAAGAACTCTAGTGGCGACATGTCTTC
AS3	ACTTGTCATCAGCACCATCAATGAAC
AS4	GATTTTGAAATCTAGACGTGGCCA
AS5	AATATCATTCTTACGATTGAACCTCTTCATATCT
5S_AS-1	ATATGGCCGCAACCT TATAGTGAGTCGTATTAG
5S_AS-2	TTACCAGCTTAACTACAGTTGATCGGACGGGAAACGGTGCTTTCTGGTAG
5S_AS-3	AGCACCTGAGTTTCGCGTATGGTCACCCACTACACTACTCGGTCAGGCTC
5S_AS-4	<i>GTTTCGTCCTCACGGACTCATCAGGACGGAGTCTAGACTCCGTCGACTGC</i>
5S_AS-5	CCCCAAGGGGTTGATCCTTGGTTA TTTTGCA
5S_AS-6	AGCTTCAAAAACCCCTCAAGACCCGTTTAGAGG
5S_AS-7	AGATTGCAGCACCTTCACAGGCTCTTAC

The T7 promoter and terminator sequences are shown in bold. The 3' end of the ribozyme sequence is shown in italics. The mutation sequences are shown in lowercase.

2.5 Structure determination

Crystallization of and data collection from a proteolytic-resistant complex comprising the N-terminal domains of Rpf2 (18–262) and Rrs1 (10–113) from *Aspergillus nidulans* were described previous section. The structure of the Rpf2-Rrs1 core complex was determined by a single wavelength anomalous diffraction (SAD) method using Se-Met substituted protein crystals with 3.5 Å resolution. All 10 selenium sites were identified and used for phasing by phenix.autosol (26). After density modification, the initial model was built by phenix.autobuild (30) and contained a single Rrs1 chain (residues17–92) and some Rpf2 fragments. This model was used for the structural analysis of the native Rpf2-Rrs1 crystal with 2.35 Å resolution by molecular replacement using phenix.automr (31). Several rounds of refinement were performed using phenix.refine (32) with manual fitting and rebuilding based on 2Fo–Fc and Fo–Fc electron density maps constructed using COOT (33). The final R_{free} and R_{work} were 23.5% and 19.2%, respectively. The final refinement statistics and geometry are summarized in Table 1-4. All figures were generated using PyMol (34). The atomic coordinates of the Rpf2-Rrs1 core complex structure has been deposited in Protein Data Bank under accession number 4XD9.

Table 1-4. Refinement statistics

Resolution range (Å)	42-2.35
Reflections work/test	36222/1909
R_{work} (%)	19.2
$R_{\text{free}}^{\text{a}}$ (%)	23.5
No. of atoms	
Protein atoms	5002
Solvent molecules	163
RMS deviations	
Bond lengths (Å)	0.003
Angles (deg)	0.910
Ramachandran plot	
Favored region (%)	97.96
Allowed region (%)	1.88
Outlier region (%)	0.16

^a R_{free} was calculated from 5% of the randomly selected reflections that were excluded from the refinement.

2.6 Gel shift assays of Rpf2-Rrs1 mutants with 5S rRNA

Full-length 5S rRNA (50 pmol) in 5 μ L of RNA buffer was mixed with increasing amounts of individual Rpf2-Rrs1 mutants (50, 100, 200 pmol) in 5 μ L of SEC buffer or dialysis buffer. After pre-incubation at 37°C for 15 min, each sample was subjected to 5% polyacrylamide (acrylamide/bisacrylamide ratio 39/1) gel electrophoresis. The electrophoresis conditions were as follows: temperature, 4°C; power voltage, 100 V; and electrophoresis buffer, 192 mM glycine and 25 mM Tris buffer. The gels were stained with ethidium bromide or Coomassie brilliant blue R-250.

2.7 Circular dichroism spectrum

Purified proteins were dialyzed against 10 mM Tris-HCl pH 7.5, 20 mM NaCl and 10% (v/v) glycerol. Circular dichroism (CD) spectra were measured on a J800 spectropolarimeter (Japan Spectroscopic Company) in a quartz cell with an optical path length of 2 mm. The CD spectra were obtained by taking the average of four scans taken in the range of 300–190 nm and normalized to molar ellipticities using the protein concentrations.

3 Results

3.1 Overall structure

A proteolysis-resistant complex of *An*Rpf2 and *An*Rrs1 (Rpf2-Rrs1 core complex), comprising residues 18–262 of *An*Rpf2 and residues 10–113 of *An*Rrs1 (Fig.1-13B), was crystallized into an orthorhombic $P2_12_12_1$ space group with the unit-cell parameters $a = 54.1$, $b = 123.3$, $c = 133.8$ Å (29). The Rpf2-Rrs1 core complex structure was determined to a resolution of 2.35 Å (Fig. 1-13A). The crystal contained two independent Rpf2-Rrs1 core complexes (complex-1: chain A-B and complex-2: chain C-D). In the crystal, chain B (Rrs1) and chain C (Rpf2) were also connected by β -sheet-type hydrogen bonds (between $\beta 3$ of Rrs1 and $\beta 2$ of Rpf2). Similarly, chain A (Rpf2) and chain D (Rrs1) were connected by the same type of hydrogen bonds. However, extensive interactions between chains A and B and chains C and D clearly identify the physiological pair. The structures of these two independent complexes were nearly identical (RMSD for all C α atoms was 0.23 Å). As the electron density for complex-1 was more clearly visible than that for the complex-2 (Residues 19–254 for Rpf2 and residues 17–104 for Rrs1 were built for complex-1, whereas two fewer N-terminal residues were built for Rrs1 of complex-2), we have described the structure based on complex-1.

Rpf2 exhibited an $\alpha + \beta$ structure. The structure comprised a wide, twisted half β -barrel in which of 10 β -strands were surrounded by four α -helices and two α -hairpins (Fig. 1-13A, 1-14). The N-terminal domain (residues 19–254) of *An*Rpf2 included the Brix domain (residues 28–245) as predicted by PROSITE (35). A structural similarity search of the DALI server revealed that Rpf2 resembles the Imp4-like protein Mil, which contains a Brix domain (Z score = 9.2, PDB ID: 1W94) (36). However, the Brix domains of Rpf2 and Mil diverged considerably (see discussion). Rrs1 was composed of a single long α -helix (residues 52–74), four short β -strands, and a long C-terminal loop (residues 88–104) (Fig. 1-13A, 1-14). The structure was mainly stabilized by interactions with Rpf2. The hydrophobic core was also formed in Rrs1 via intra-molecular interactions of the conserved residues on the C-terminal region of the helix and the residues at the loop region (L33, L36, A38, L67, L71 and L88). The long α -helix was also stabilized via intra-molecular hydrogen bonds between largely conserved side chains (Q65-N69, Q65-R61 and R61-D62).

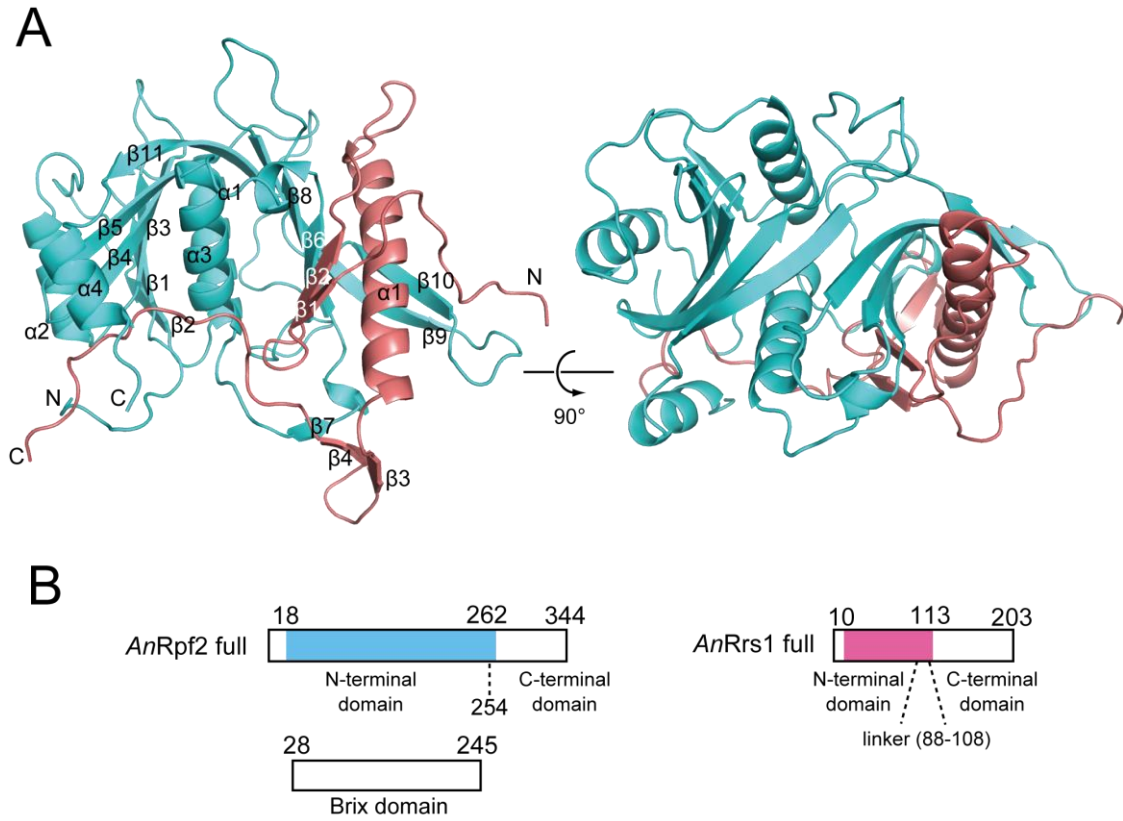


Fig. 1-13 Overall structure of the Rpf2-Rrs1 core complex. Rpf2 and Rrs1 are shown in cyan and pink, respectively. (A) Ribbon diagram of the Rpf2-Rrs1 core complex viewed from the front (left) and top (right) of the complex. (B) Schematic drawings indicating each domain. The proteolysis resistant complex (Rpf2-Rrs1 core complex) used for this experiment is indicated by color regions.

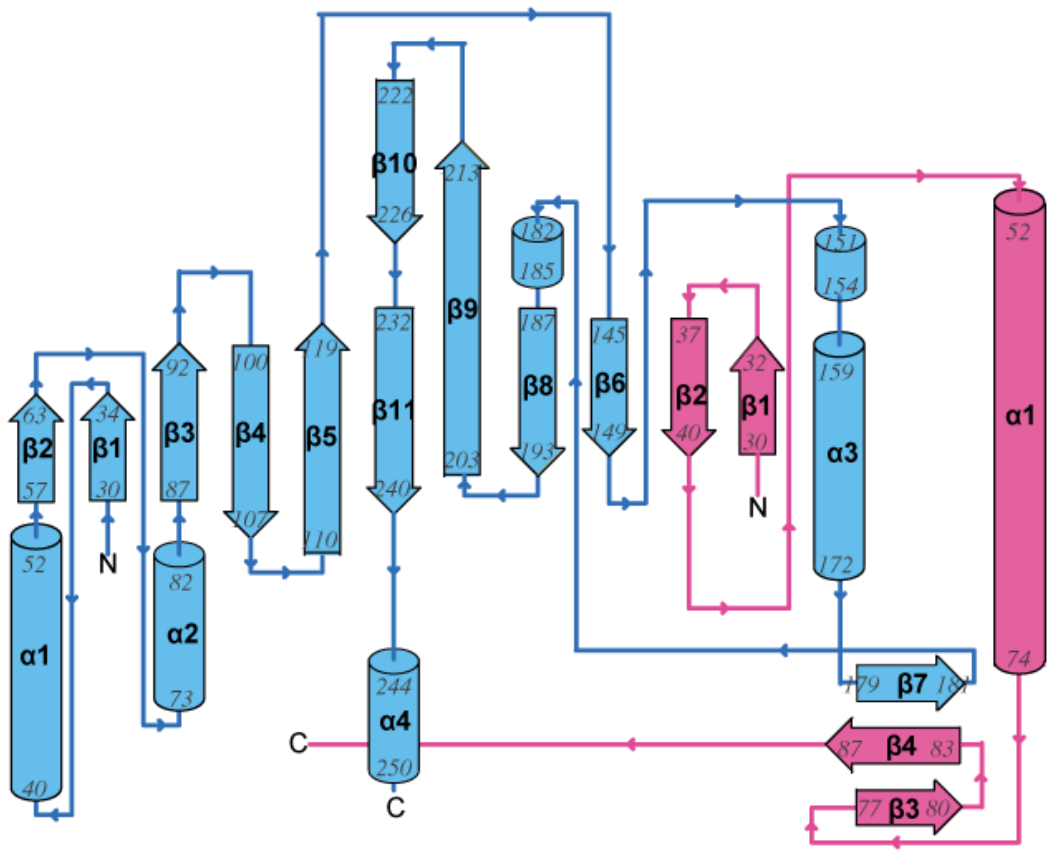


Fig. 1-14 Topology diagram indicating the secondary structure. Rpf2 and Rrs1 are shown in cyan and pink, respectively. Helices and beta strands are numbered.

3.2 Detailed interaction between Rpf2 and Rrs1

The two proteins were so intimately connected that they resembled a single molecule. Three regions contributed to the molecular interactions between Rpf2 and Rrs1. These were the long α -helix (α 1), β -sheets and C-terminal proline-rich loop (residues 88–104) of Rrs1. The amphiphilic long α -helix of Rrs1 formed both hydrophobic and hydrophilic interactions with the wide β -sheet of Rpf2. A hydrophobic surface was formed by seven residues (L56, A60, V64, L67, L68, L71 and L72) on the α -helix of Rrs1. These residues were involved in hydrophobic interactions with the hydrophobic surface created by ten residues in Rpf2 (L145, L147, L185, A188, M190, I211, L220, P221, V223 and L225) (Fig. 1-15A). Most of these residues are conserved across eukaryotes. The hydrophilic surface of the Rrs1 α -helix was formed by five residues (N53, K57, R61, Q65, and N69). The side chains of K57, R61 and Q65 of Rrs1 formed hydrogen bonds with three main-chain oxygens of Rpf2 (P221, V223, and L225). The side-chain of Q65 formed an additional hydrogen bond with the amide nitrogen of V223 on a β -sheet of Rpf2. A hydrogen-bonded side chain interaction was observed between the N53 of Rrs1 and R207 of Rpf2 (Fig. 1-15B). The N69 of Rrs1 also formed an intra-molecular hydrogen bond with I21 on the N-terminal loop.

Two β -strands (β 1, β 2) of Rrs1 joined the central β -sheet of Rpf2 to complete the 12-stranded β -barrel structure, and the other two β -strands (β 3, β 4) formed a three-stranded β -sheet with the β 7 strand of Rpf2 (Fig. 1-14).

The long C-terminal loop of Rrs1 wrapped around the side of Rpf2 (Fig. 1-13A, 1-16). This loop is highly conserved in eukaryotes; among the 17 residues in the loop (88-104), nine (L88, P89, P91, T93, L95, P96, R97, K99, and P102) are completely conserved. This loop is rich in proline residues that are either completely conserved (shown above) or highly conserved (P100 and P104) (Fig. 1-17). Most of the conserved residues are involved in either intra- or inter-molecular interactions. The T93 of Rrs1 forms intra-molecular hydrogen bonds with the side-chain of D32 (Fig. 1-16). Three residues (P96, R97 and K99) of Rrs1 form hydrogen bonds with three main-chain carbonyl oxygens (Q22, L23 and A250) and three conserved side chains (E25, K28 and D84) of Rpf2 (Fig. 1-18). These conserved interactions between Rpf2 and Rrs1 suggest the importance of the proline-rich loop to be fixed at this region. This conserved proline rich loop likely plays a role in locating the C-terminal domain of Rrs1 at the opposite side of the N-terminal domain with respect to Rpf2.

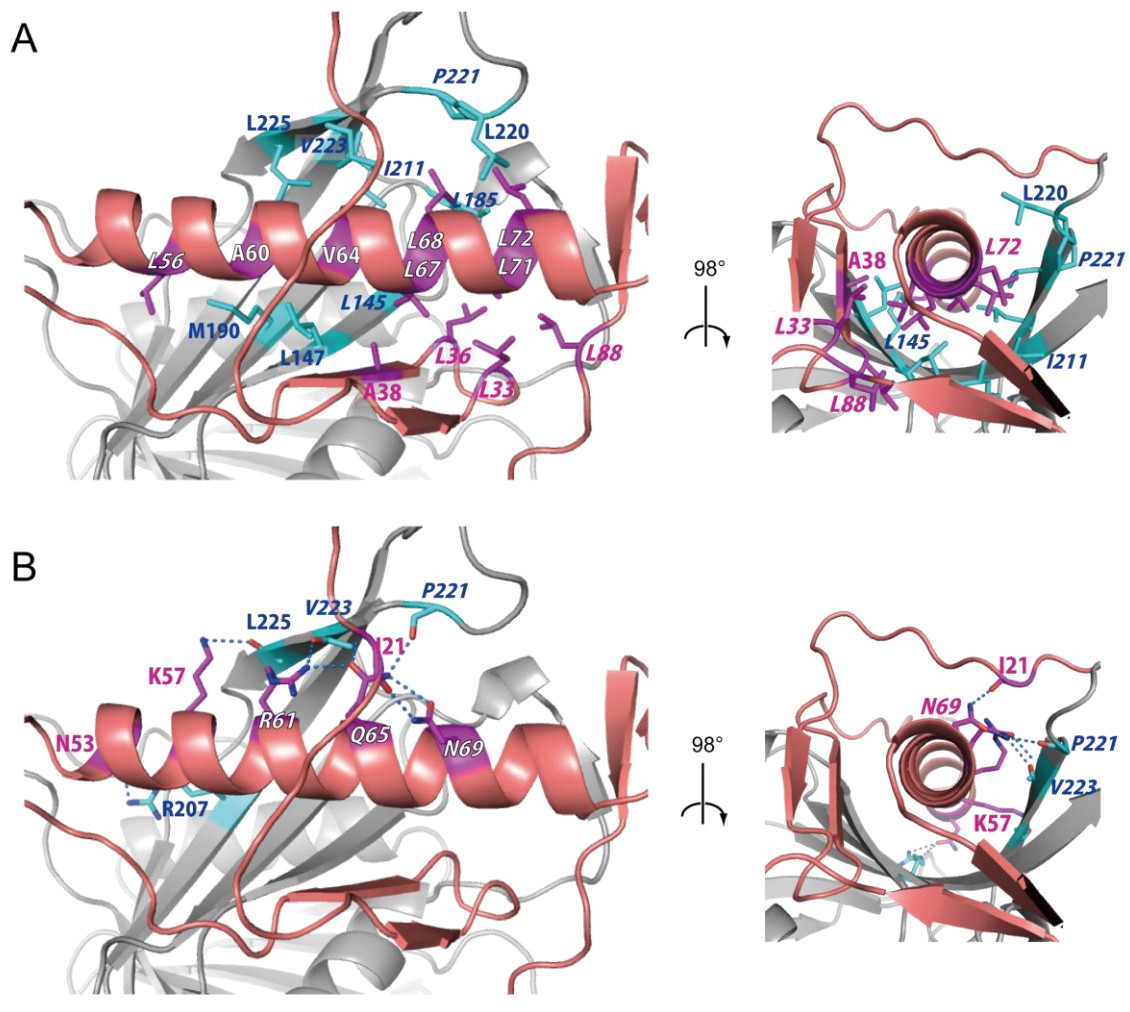


Fig. 1-15 Interactions between Rpf2 and Rrs1. (A, B) Dimerization interface between the long α -helix of Rrs1 and wide β -sheet of Rpf2. Residues of Rrs1 (purple) and Rpf2 (cyan) involved in the interactions are displayed as stick models and labeled. (A) Hydrophobic interactions. (B) Hydrogen-bonding interactions.

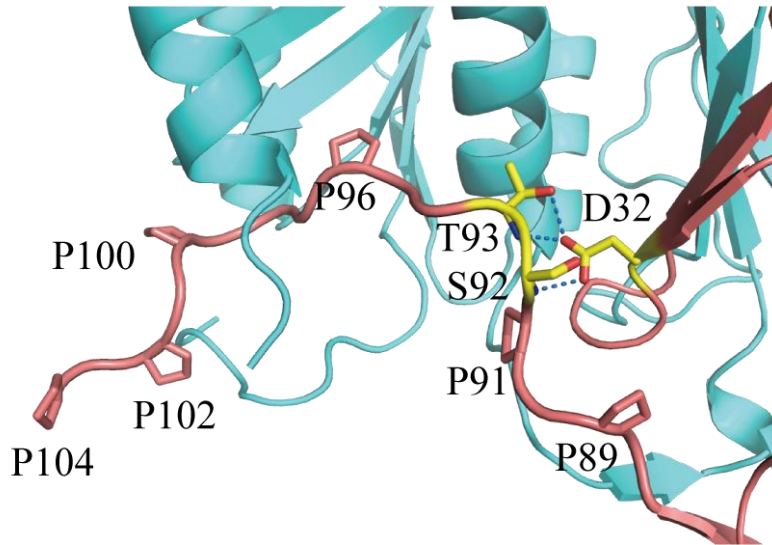


Fig. 1-16 Close-up view of the C-terminal proline-rich loop of Rrs1. Prolines are labeled and displayed as stick models. Side chains of D32, S92 and T93 from Rrs1 form intra-molecular hydrogen bonds. These three residues are labeled and displayed as yellow stick models.

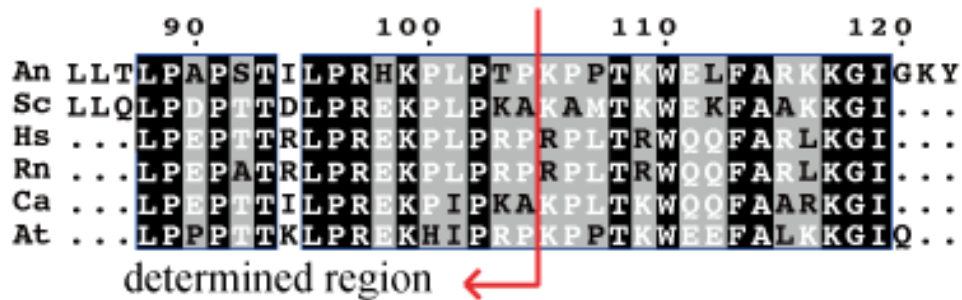


Fig. 1-17 Sequences in the proline-rich loop after CLUSTALW alignment (37). The sequences are as follows: An; *Aspergillus nidulans*, Sc; *Saccharomyces cerevisiae*, Hs; *Homo sapiens*, Rn; *Rattus norvegicus*, Ca; *Candida albicans*, At; *Arabidopsis thaliana*. The most conserved sites are highlighted in black. Red arrow indicates the region for which the structure was determined. This figure was prepared using the program ESPript (38).

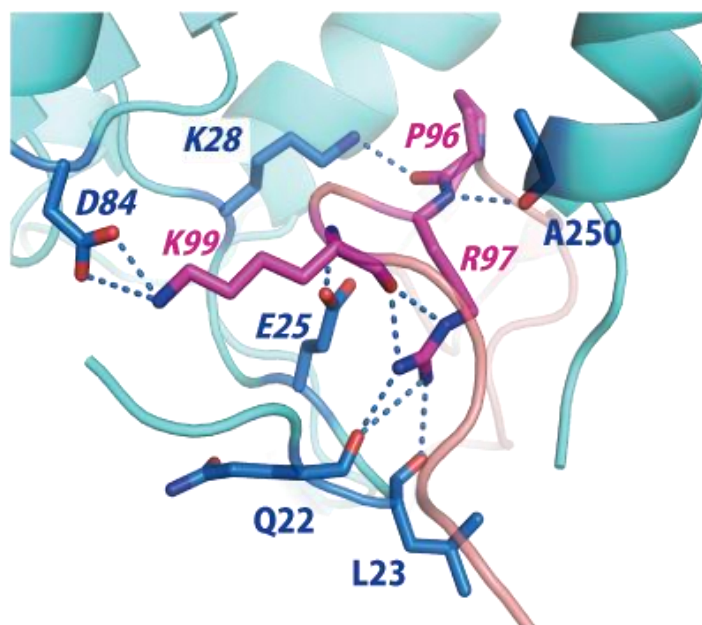


Fig. 1-18 Close-up view of hydrogen-bonding interactions at the C-terminal loop of Rrs1. Amino acid residues that form the interaction are displayed as stick models. Conserved residues are denoted in *Italics*.

3.3 5S rRNA binding assay for Rpf2- Rrs1 complex

The N-terminal domain of Rpf2 (residues 19–254) included the Brix domain (residues 28–245) (Fig. 1-13B). As this domain is known as an RNA binding domain, it can be inferred that the Rpf2-Rrs1 complex contains a site for 5S rRNA binding. To confirm this functionality, a gel shift assay was performed in the presence of increasing amounts of Rpf2-Rrs1 complexes that had been pre-incubated with 5S rRNA. Because eukaryotic ribosome biogenesis has been studied most extensively in yeast, we used *Saccharomyces cerevisiae* proteins and RNA for this experiment. The sequences of Rpf2 and Rrs1 are highly conserved between *A. nidulans* and *S. cerevisiae* (sequence identities of Rpf2 and Rrs1: 38.24% and 41.45%, respectively). As the amount of Rpf2-Rrs1 increased, bands corresponding to the 5S rRNA disappeared and bands corresponding to the Rpf2-Rrs1-5S rRNA complex appeared. This result indicated that the Rpf2-Rrs1 complex could bind to 5S rRNA (Fig. 1-19B).

To characterize the binding feature, we used three C-terminal deletion complexes (*ScRpf2* Δ C-Rrs1, *ScRpf2*-Rrs1 Δ C, *ScRpf2* Δ C-Rrs1 Δ C) in binding experiments (Fig. 1-19A). All deletion complexes exhibited the 5S rRNA complex bands observed with the full-length Rpf2-Rrs1 complex (Fig. 1-19C, D, E). These results revealed that the N-terminal core complex alone could bind 5S rRNA. However, since the bands of 5S rRNA remained at the highest concentration of proteins, the C-terminal domains also appear to be involved in 5S rRNA binding. For the *ScRpf2*-Rrs1 and *ScRpf2* Δ C-Rrs1 complexes, an extra band at a higher molecular weight than the 5S rRNA complex was also observed at a higher protein concentration (Fig. 1-19B, D); however, these bands were not detected with the *ScRpf2*-Rrs1 Δ C complex, suggesting that the C-terminal domain of Rrs1 was involved in oligomerization.

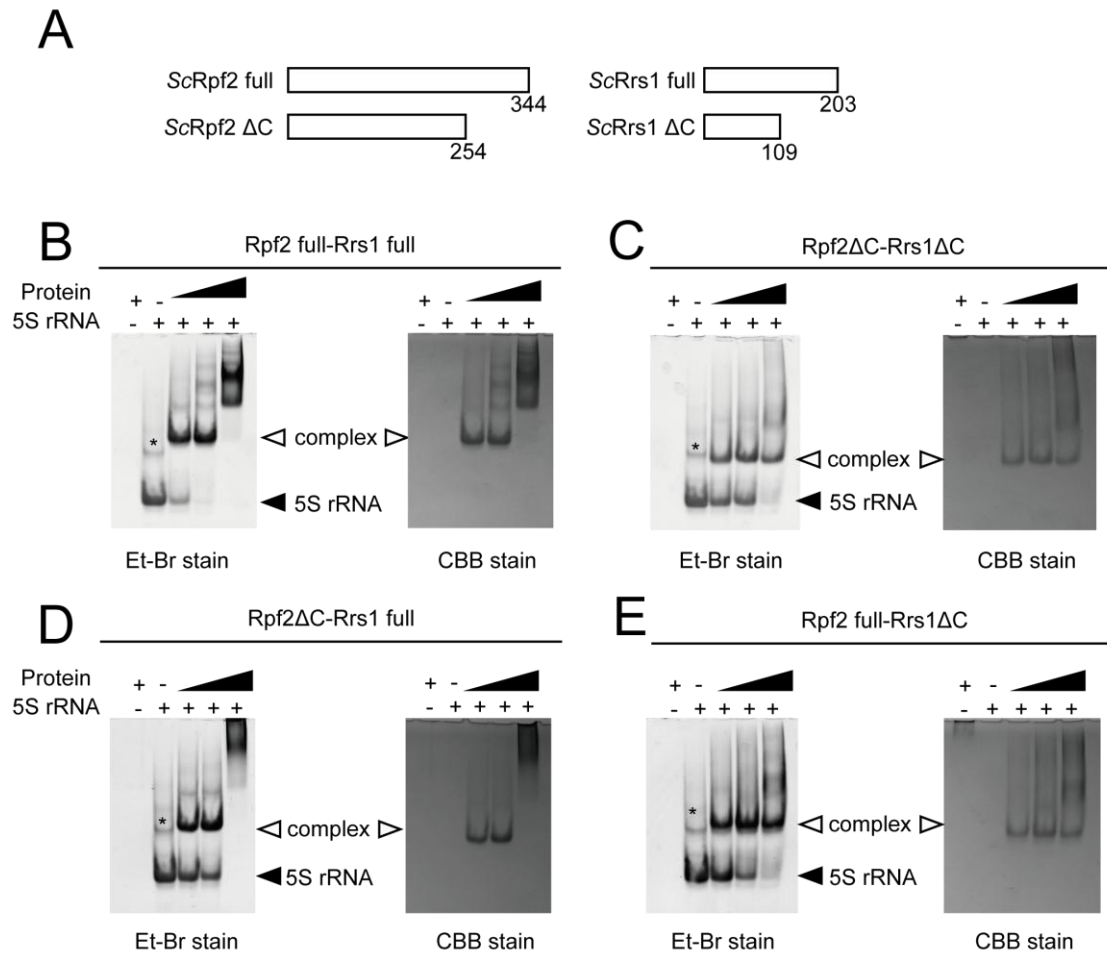


Fig. 1-19 5S rRNA binding assay. (A) Schematic overview of the Rpf2 and Rrs1 variants. (B-E) Results of the gel shift assay. *Sc*5S rRNA (50 pmol) was incubated without factor or with 50, 100, and 200 pmol of *Sc*Rpf2-Rrs1 complex variants: *Sc*Rpf2 full-Rrs1 full (B), *Sc*Rpf2ΔC-Rrs1ΔC (C), *Sc*Rpf2ΔC-Rrs1 full (D), *Sc*Rpf2 full-Rrs1ΔC (E). Asterisk (*) indicates the 5S rRNA dimer. Each gel was stained with ethidium bromide (Et-Br stain, left) and Coomassie Brilliant Blue (CBB stain, right).

3.4 Structural elements involved in binding between the Rpf2-Rrs1 complex and 5S rRNA

A detailed inspection of the complex surface in terms of sequence conservation and surface potentials highlighted four possible regions for 5S rRNA binding on Rpf2 (Fig. 1-20A, B). Based on these results, we prepared various mutation variants of these regions and inspected the 5S rRNA binding abilities (Fig. 1-21, Table 1-2). The substitution of alanine for all residues in region-1 (R62, K63), region-3 (K94, K95 and R96), and region-4 (R236) partially disrupted the binding to 5S rRNA (Fig. 1-22-3, 4). On the other hand, no effect was detected for region-2 (K81) mutants (Fig. 1-22-2). A combined region-3 and -4 mutation drastically affected the interaction with 5S rRNA (Fig. 1-22-5). The other two combination mutants yielded similar results (Fig. 1-22-6, 7). A triple-region mutation completely disrupted binding to 5S rRNA (Fig. 1-22-8), indicating that R62, K63, K94, K95, R96, and R236 are important residues for the interaction between Rpf2-Rrs1 and 5S rRNA. Among these, the R236 of *ScRpf2* (R238 of *AnRpf2*) might be most important for the interaction with 5S rRNA, as a single amino acid mutation significantly reduced the binding ability. Indeed, this residue is located on a σ^{70} -like motif that is reportedly involved in RNA binding (11). Moreover, a cation- π interaction was observed between R238 and F70 in our structure (Fig. 1-23). Alanine mutations of the conserved residues P69, F70, and E71 (corresponding to P68, F69, and E70 of *ScRpf2*) disrupted binding to 5S rRNA (Fig. 1-24), although its tertiary structure did not significantly differ from the wild type as detected from the CD spectra (Fig. 1-25).

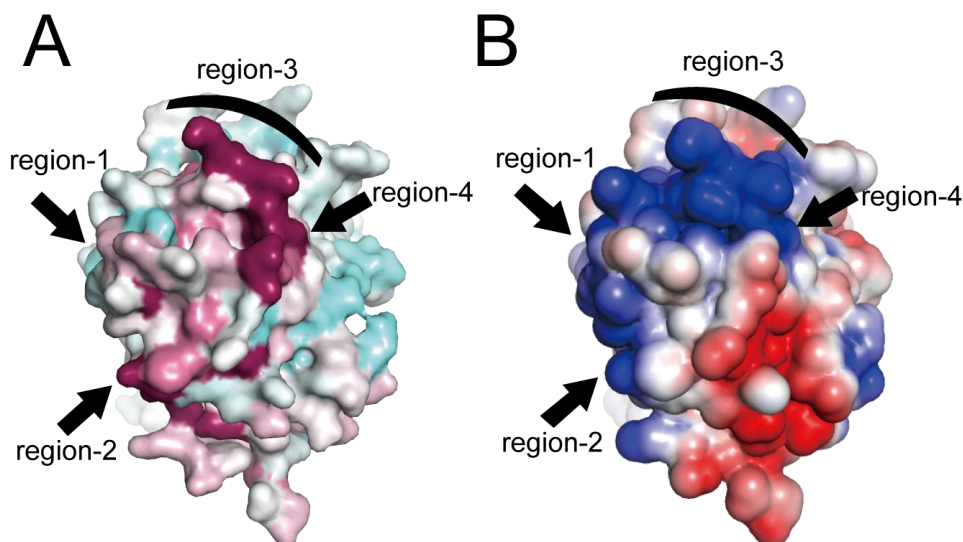


Fig. 1-20 Evolutionarily conserved and electrically positive regions of ScRpf2 (region-1 to 4) were selected for mutagenesis experiments to test the significance of the interactions with 5S rRNA. These figures were produced using Consurf (39) and APBS (40). (A) Sequence conservation is mapped onto the surface along with variable (cyan) and conserved (purple) residues. (B) Electrostatic surface potential diagrams with positive (blue) and negative (red) electrostatic potentials are mapped onto a van der Waals surface diagram of the conserved surface patch. The color scale ranges between $-3 k_B T$ (red) and $+3 k_B T$ (blue), where k_B is Boltzmann's constant and T is temperature.

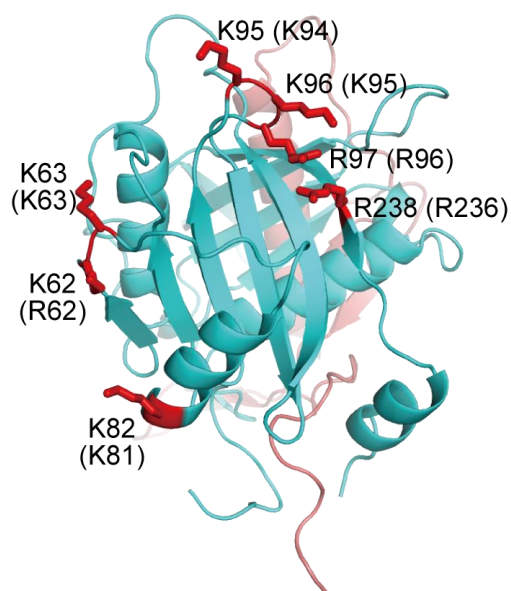


Fig. 1-21 Ribbon diagram of the Rpf2-Rrs1 core complex in the same orientation as in Fig. 1-20A and B. Four regions containing seven residues (red) were selected for mutation analysis. Letters in parentheses correspond to the residue numbers for ScRpf2.

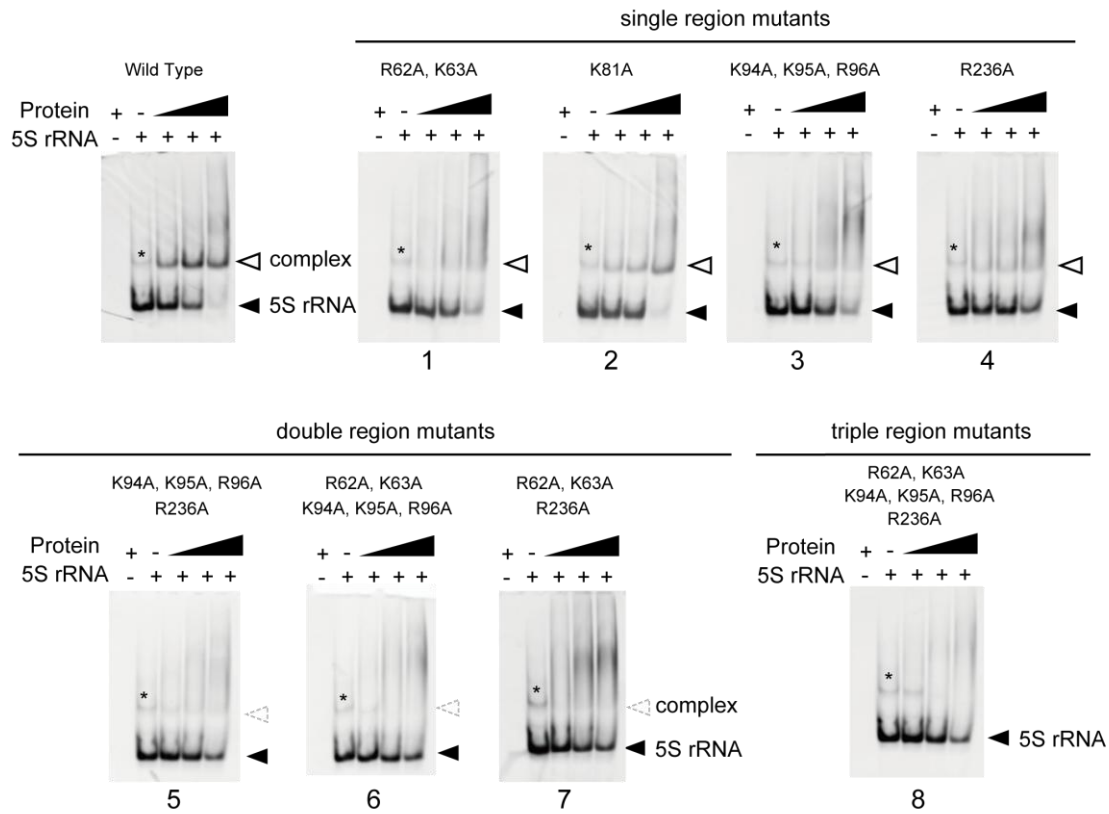


Fig. 1-22 Results of the gel shift assay. *Sc*5S rRNA (50 pmol) was incubated without factor or with 50, 100, or 200 pmol of *Sc*Rpf2-Rrs1 complex mutated variants; the denoted numbers correspond to the mutant No. (Table 1-2). Wild type indicates *Sc*Rpf2 Δ C-Rrs1 Δ C purified using the same method used to purify other point-mutated variants. Asterisk (*) indicates the 5S rRNA dimer. Results are shown as an ethidium bromide-stained gel.

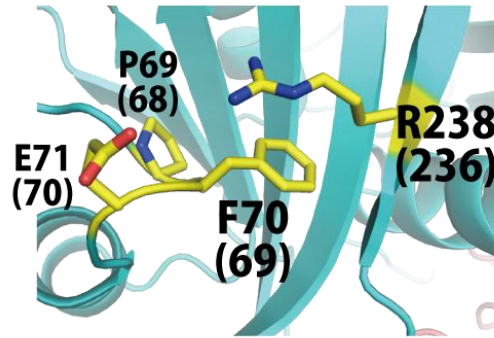


Fig. 1-23 Close view of the contact between R238 and F70. Letters in parentheses correspond to residue numbers for *ScRpf2*.

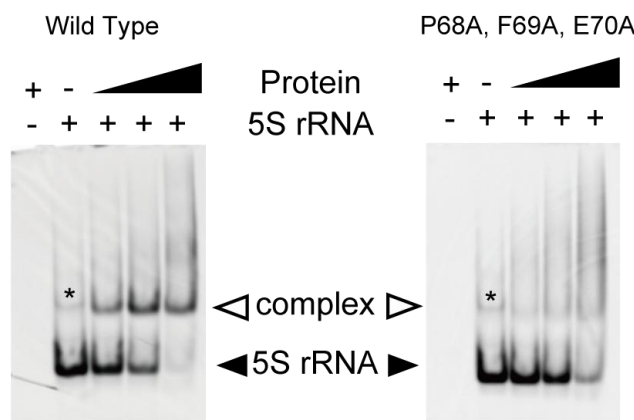


Fig. 1-24 Results of a gel shift assay with wild type (left) or mutant 9 (right), in which alanine substitutes for P68, F69 and E70. *Sc5S* rRNA (50 pmol) was incubated without factor or with 50, 100, and 200 pmol of *ScRpf2*-Rrs1 complex. Wild type indicates *ScRpf2* Δ C-Rrs1 Δ C purified using same method used to purify other point-mutated variants. Asterisk (*) indicates the 5S rRNA dimer.

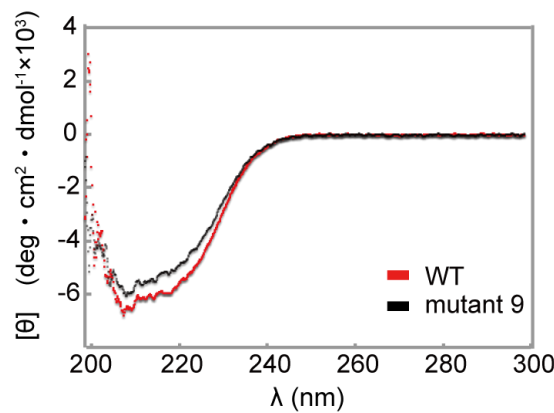


Fig. 1-25 CD spectra of the *ScRpf2*-Rrs1 complex. Red line; wild type, Black line; mutant 9.

4 Discussion

4.1 Structural aspect of full-length Rpf2-Rrs1 complex

In this study, we reported the crystal structure of the *An* Rpf2-Rrs1 core complex (Rpf2 [residues 18–262]-Rrs1 [residues 10–113]). This is the core region of the Rpf2-Rrs1 complex as suggested by its resistance against proteolytic digestion (29). The structural analysis revealed that these N-terminal domains of Rpf2 and Rrs1 bind each other tightly. PSIPRED programs for predicting secondary structures (27) suggested that the C-terminal region of Rpf2 is a flexible loop (approximately 80 residues). On the other hand, the C-terminal region of Rrs1 was predicted to have a secondary structure, suggesting that the intact Rrs1 comprises two similarly sized domains connected by a central proline-rich linker region (residues 88–108). Therefore, the intact Rpf2 and Rrs1 molecules appear to work with the anchoring core domains of the N-terminal regions as well as the peripheral C-terminal regions.

4.2 Rpf2/Brix domain as a highly evolutionarily modified scaffold domain

The Rpf2/Brix domain includes a half- β -barrel surrounded by three α -helices and two α -hairpins. The N- and C-terminal halves of the Brix domain are thought to have evolved by means of gene duplication. Indeed, the N- and C-terminal halves of Mil exhibited a similar architecture (Fig.1-26 D, E) (20). In the Rpf2/Brix domain, although the folding topologies were conserved between the N- (19–139) and C- (residues 140–240) terminal halves, the appearances of the two structures were extensively divergent (Fig.1-26 A, B). Interestingly, the long α -helix of Rrs1 appeared to correspond with the C-terminal half of Rpf2/Brix domain; the α 1 and β 2 of Rrs1 correspond to α 2 and β 2 of the N-terminal half of the Rpf2/Brix domain, respectively (Fig.1-26 A, C). These structural features suggest that the C-terminal half of the Rpf2/Brix domain underwent extensive evolution after gene duplication through the addition of extra regions and replacement of the α -helix with that of Rrs1.

The Brix domain contains a σ^{70} -like RNA binding motif between β 10 and β 11 (*An*Rpf2: 223-240) (11). The structure of the Rpf2-Rrs1 core complex demonstrated that this motif comprises a sheet-turn-sheet structure and is located at the center of the Brix domain. The finding that the R238 on this motif was significant for 5S rRNA binding (as mentioned above) is consistent with the findings of a previous study (11). In addition, V223 and L225 on this motif were shown to be involved in binding to Rrs1, suggesting that this motif includes an important region for binding both RNA and proteins.

The Brix domain is known as a scaffold domain. Each protein containing this domain is associated with a specific partner. The present study showed that the N-terminal half of the Rpf2/Brix domain bound to 5S rRNA and the C-terminal half bound to Rrs1. However, R220 and R253 in C-terminal half of the *ScImp4*/Brix domain has been reported as important for the association with U3 snoRNA (41). Therefore, the Brix domain has undergone significant specialization through evolution while retaining its core structure.

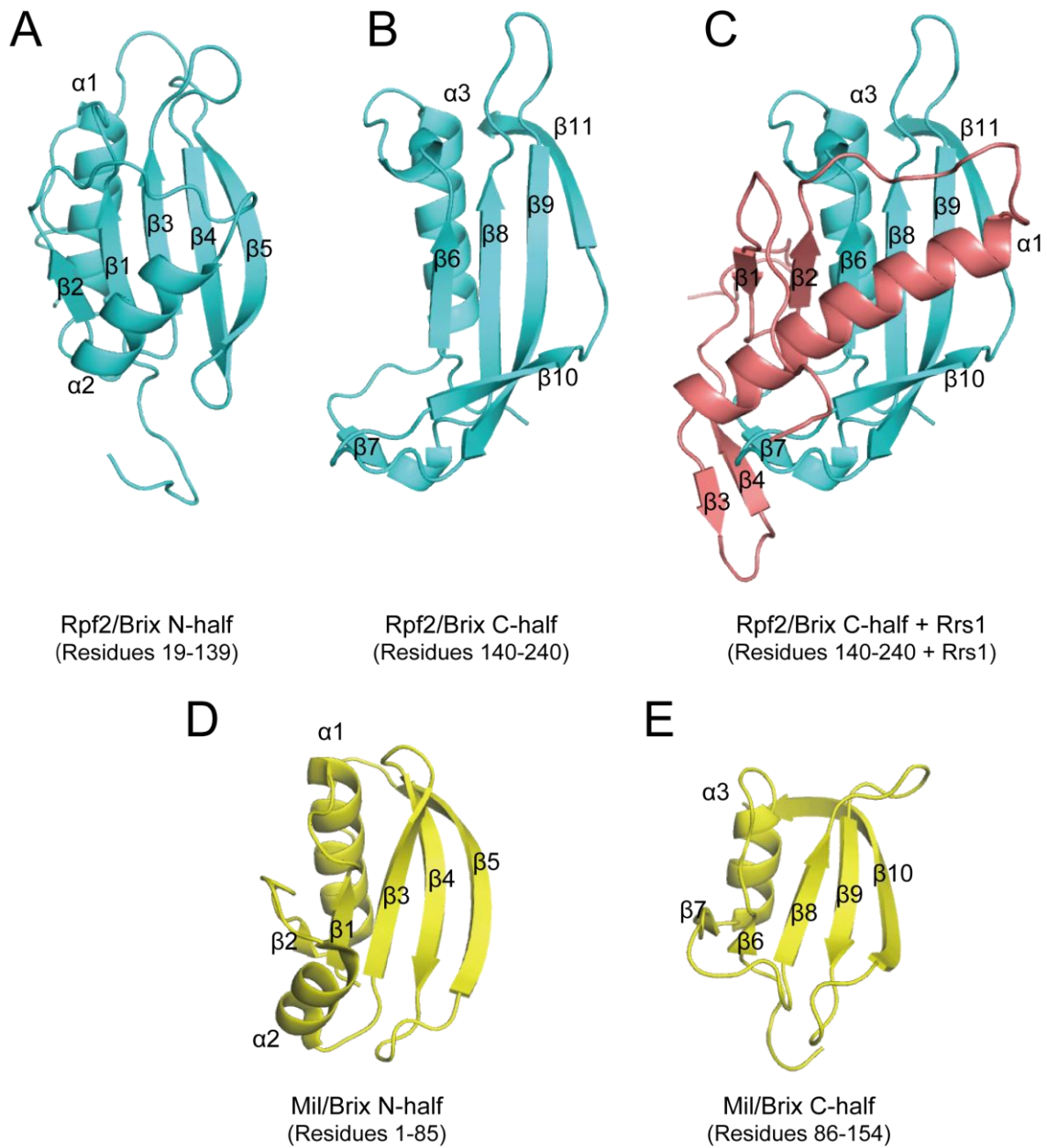


Fig. 1-26 Structural comparison of the N- and C-terminal halves of the Brix domains. (A, B) N- and C-terminal halves of Rpf2/Brix domain and (C) C-terminal half of Rpf2/Brix domain plus Rrs1. The long α -helix of Rrs1 appears to correspond with the C-terminal half of the Rpf2/Brix domain. (D, E) The N- and C-terminal halves of Mil Brix, showing the duplicated architecture. Rpf2, Rrs1, and Mil are colored in cyan, pink, and yellow, respectively.

4.3 Role of Rrs1 and proline-rich linker

The N-terminal domain of *AnRrs1* (residues 19–104), which was determined in the present study, is closely related to the cold-sensitive mutant *rrs1-1* of *ScRrs1* (residues 1–113). Although *rrs1-1* causes a defect in rRNA processing at low temperatures, it is viable at temperatures higher than 25°C (14,21), suggesting that the N-terminal domain of Rrs1 itself plays a significant role in its function. Our present results showed that the N-terminal domain of Rrs1 played a role in ribosome biogenesis via interaction with the N-terminal domain of Rpf2. In addition, yeast-two hybrid assays showed that the *ScRrs1* L65P mutant inhibited the associations with two ribosomal proteins (RpL5 and RpL11) (15). This residue corresponds to L71 of *AnRrs1* and is located on the C-terminal portion of the long α -helix. As proline has been noted as α -helix breaker, the substitution of proline for leucine in the α -helix caused partial disruption of the C-terminal region of the helix. Consequently, Rrs1 might have lost its capacity to bind RpL5 and RpL11. Taken together, these facts suggest that the N-terminal domain of Rrs1 is an important adaptor domain for the interactions with Rpf2, RpL5 and RpL11.

It is generally accepted that eukaryotic inter-domain linkers have rather tight structures (e.g., helical or proline-rich structures) and act as rigid spacers to prevent unfavorable interactions between two domains (42). Actually, the deletion or shortening of linker segments sometimes prohibits their function (43-45). Similarly, in Rrs1, the linker region connecting the N- and C-terminal domains comprises a conserved proline-rich segment (88–107) (Fig.1-27). This chain segment runs along the molecular surface of Rpf2 (Fig. 1-16). Highly specific interactions were observed between the conserved residues at the ending position of the linker and the conserved residues of Rpf2 (Fig. 1-18). A mutant (*AnRrs1* residues 1-90) lacking this region retained the capacity to bind Rpf2 (data not shown), suggesting that these conserved interactions are not required for the binding of two N-terminal domains. Therefore, it is likely that these conserved interactions are used to anchor the terminal region of the linker at a specific position on Rpf2. These facts suggest that the C-terminal domain of the Rrs1 linker localizes on a specific Rpf2 site (i.e., a site remote from the N-terminal domain of Rrs1). The results of a binding assay with 5S rRNA indicated that Rpf2 full-Rrs1 Δ C had a lower binding affinity for 5S rRNA relative to Rpf2 full-Rrs1 full, indicating that the Rrs1 C-terminal domain assists in the interaction with 5S rRNA. Taken together, the N- and C-terminal domains of Rrs1 are arranged on separate positions of Rpf2 via a proline-rich linker and play distinct roles in ribosome biogenesis.

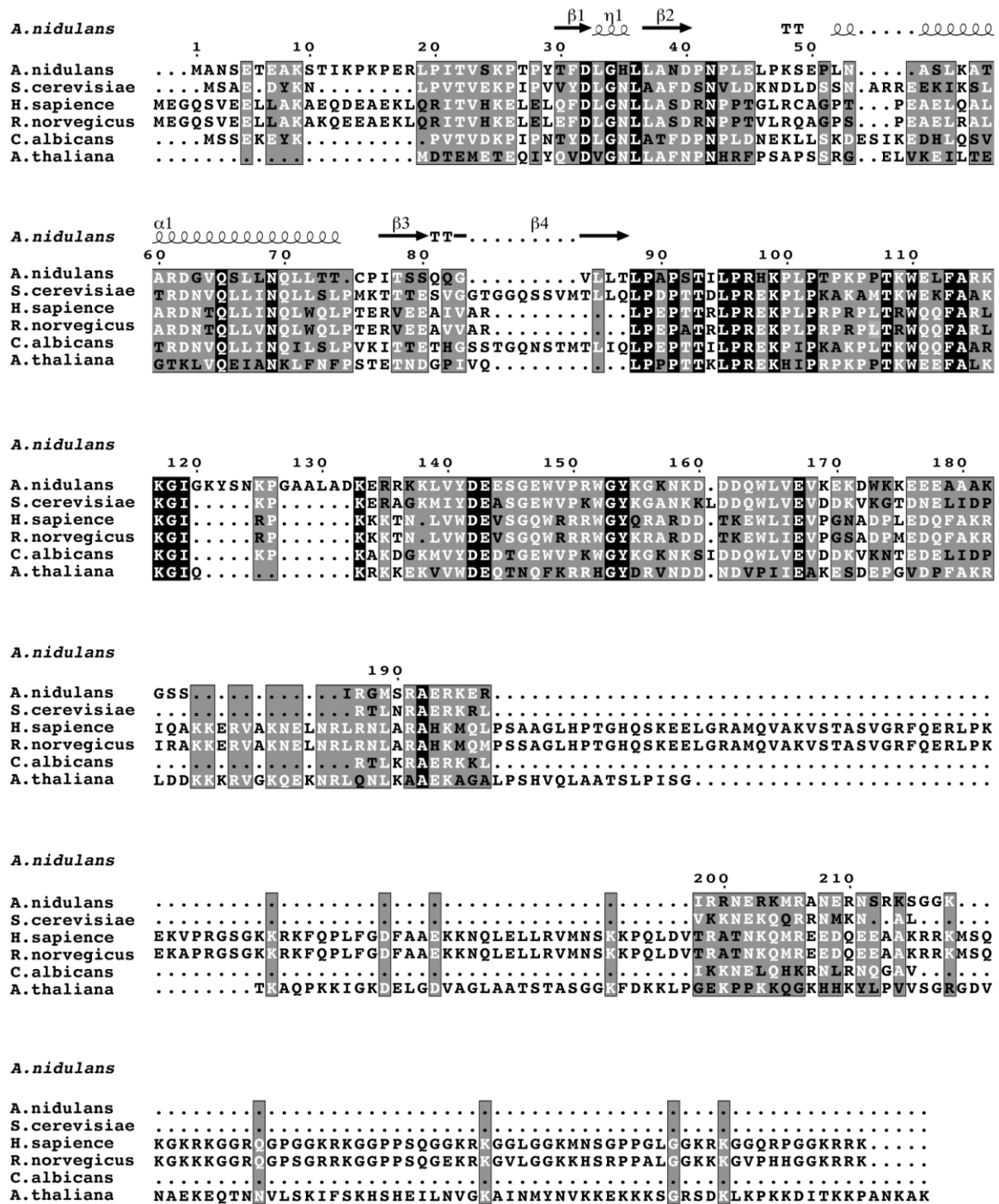


Fig. 1-27 Rrs1 amino acid sequence alignment. The sequences displayed are as follows: *A. nidulans*, *Aspergillus nidulans*; *S. cerevisiae*, *Saccharomyces cerevisiae*; *H. sapiens*, *Homo sapiens*; *R. norvegicus*, *Rattus norvegicus*; *C. albicans*, *Candida albicans*; *A. thaliana*, *Arabidopsis thaliana*. The most conserved sites are highlighted in black. Each protein sequence was aligned using CLUSTALW, and the figure was prepared with the program ESPrnt. Secondary structure elements of the *A. nidulans* Rrs1 N-terminal domain are also shown.

4.4 Binding model of Rpf2-subcomplex with 90S ribosome

The structural analysis of the Rpf2-Rrs1 complex together with a previous functional analysis suggested that the C-terminal part of the long α -helix of Rrs1 associates with RpL5 and RpL11 and that the conserved basic patch on Rpf2 recognizes 5S rRNA. As the eukaryotic ribosomal structure has been analyzed and the binding manners of 5S rRNA, RpL5 and RpL11 are known (2), we attempted to construct a complex model containing five molecules (Rpf2-subcomplex) by docking the Rpf2-Rrs1 core complex on the tripartite complex (5S rRNA-RpL5-RpL11). For this model, the Rrs1 region that binds with RpL5 and RpL11 was located in the vicinity of RpL5 and RpL11 in the 5S rRNA-RpL5-RpL11 complex. Furthermore, the Rpf2 basic patch that binds with 5S rRNA was located near 5S rRNA in the 5S rRNA-RpL5-RpL11 complex. In this model, Rpf2-Rrs1 was snugly situated at the inside of the curved region of 5S rRNA (Fig. 1-28). This Rpf2-subcomplex model satisfied the results of the binding assay that revealed direct interactions within each pair formed by the molecules Rrs1, Rpf2, RpL5 and RpL11 (10,12-15). In addition, in the model both the C-termini of Rpf2 and Rrs1 (Rpf2: G254, Rrs1: P104) were positioned at the 5S rRNA side. This observation accounted for the results of the gel shift assay involving C-terminal deletion complexes, which suggested that both C-terminal domains were involved to some extent in the interactions with 5S rRNA.

Rpf2 and Rrs1 are localized on 90S and pre-60S particles in the nucleolus and are involved in 27SB rRNA processing (11,12). Although the structure of the nuclear ribosome precursor has not yet been determined, a recent cryo-electron microscopy study revealed the structure of the cytoplasmic pre-60S particle in which 5S rRNA is rotated nearly 180° relative to the mature subunit (PDB code: 4V7F) (46). The Rpf2-subcomplex model was superposed on the 5S rRNA-RpL5-RpL11 of this pre-60S particle, suggesting that the Rpf2-Rrs1 complex is located between 5S rRNA and the ribosome precursor (Fig. 1-29). This indicates that the Rpf2-Rrs1 complex can associate directly with the 90S precursor even after Rpf2-subcomplex formation. Furthermore, this model demonstrates that a wide, positively charged region of Rpf2 faces the ribosome precursor and that the Rpf2-Rrs1 complex occupies the 25S rRNA binding regions of RpL5 and RpL11, suggesting that instead of these proteins, the Rpf2-Rrs1 complex might associate with pre-rRNA on the 90S precursor.

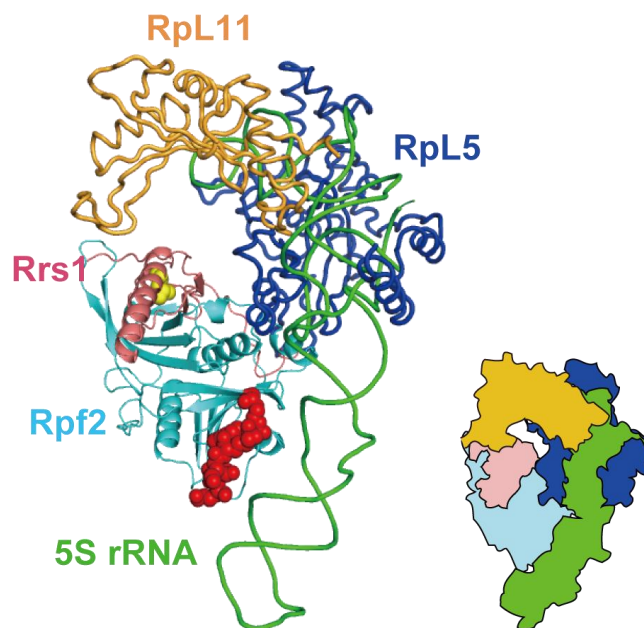


Fig. 1-28 Rpf2-subcomplex model. (A) Rpf2-subcomplex model (left) and schematic representation (right). Red spheres represent the 5S rRNA binding region on Rpf2. Yellow spheres represent the RpL5 and RpL11 interaction region on Rrs1. The molecules are colored as follows: cyan, Rpf2; pink, Rrs1; green, 5S rRNA; light orange, RpL11; blue, RpL5.

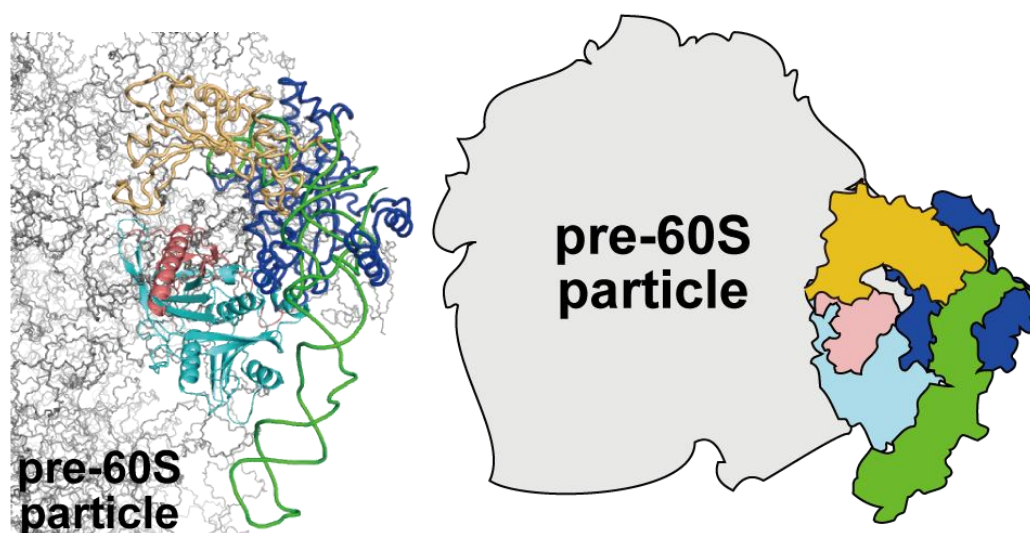


Fig. 1-29 Rpf2-subcomplex model superposed on the ribosomal precursor (left); schematic representation (right). The molecules are colored as follows: cyan, Rpf2; pink, Rrs1; green, 5S rRNA; light orange, RpL11; blue, RpL5; gray, pre-60S particle.

Chapter II

Study on EFL1 and SBDS relating in final maturation step of pre-60S in cytoplasm

Summary

Removal of anti-association factor, Tif6 (eIF6), by elongation factor-like 1 (EFL1) and Shwachman–Bodian–Diamond syndrome (SBDS) protein is a critical step in the late stage of ribosome maturation. Although EFL1 is known to have GTPase activity that is stimulated by SBDS, how they cooperatively trigger dissociation of Tif6 from the ribosome remains to be elucidated.

In the present study, the interaction between EFL1 and SBDS was analyzed by size exclusion chromatography, gel shift assay, and isothermal titration calorimetry (ITC). The results showed that EFL1 interacted directly with SBDS. ITC experiments using domain truncated mutants showed that the interaction between EFL1 and SBDS is governed by the insertion domain of EFL1 and domains II – III of SBDS. Circular dichroism spectroscopy showed that the insertion domain of EFL1 has a random structure in the absence of SBDS, whereas the disadvantageous entropy change observed on ITC suggested a fixed conformation coupled with complex formation with SBDS. Based on these observations together with those reported previously, I propose roles of EFL1 and SBDS in ribosomal maturation.

1 Introduction

1.1 Final maturation step of pre-60S in cytoplasm

Eukaryotic ribosomes are preassembled in the nucleus and mature in the cytoplasm. Tif6 is one of the “B-factors” which have been shown to be necessary for the processing of 27SB pre-rRNA (47). The removal of Tif6—the yeast homolog of mammalian eukaryotic translation initiation factor 6 (eIF6)—is critical for late cytoplasmic maturation of the 60S ribosomal subunit (47). Tif6 acts as a ribosomal anti-association factor, which binds to the pre-60S subunit to inhibit subunit joining by steric hindrance (48-50). Therefore, dissociation of Tif6 from pre-60S ribosome is essential for enabling assembly into the 80S subunit. Genetic studies in *Saccharomyces cerevisiae* indicated that SBDS and GTPase elongation factor-like 1 (EFL1) function cooperatively in this releasing pathway (51). Biochemical analysis showed that 60S-ribosome dependent GTP hydrolysis of EFL1 was stimulated by SBDS, and SBDS and EFL1 directly catalyzed Tif6 removal by a mechanism that required hydrolysis of GTP by EFL1 (52) (Fig. 2-1). However, it remains to be elucidated how EFL1 and SBDS cooperatively trigger dissociation of Tif6 from the ribosome.

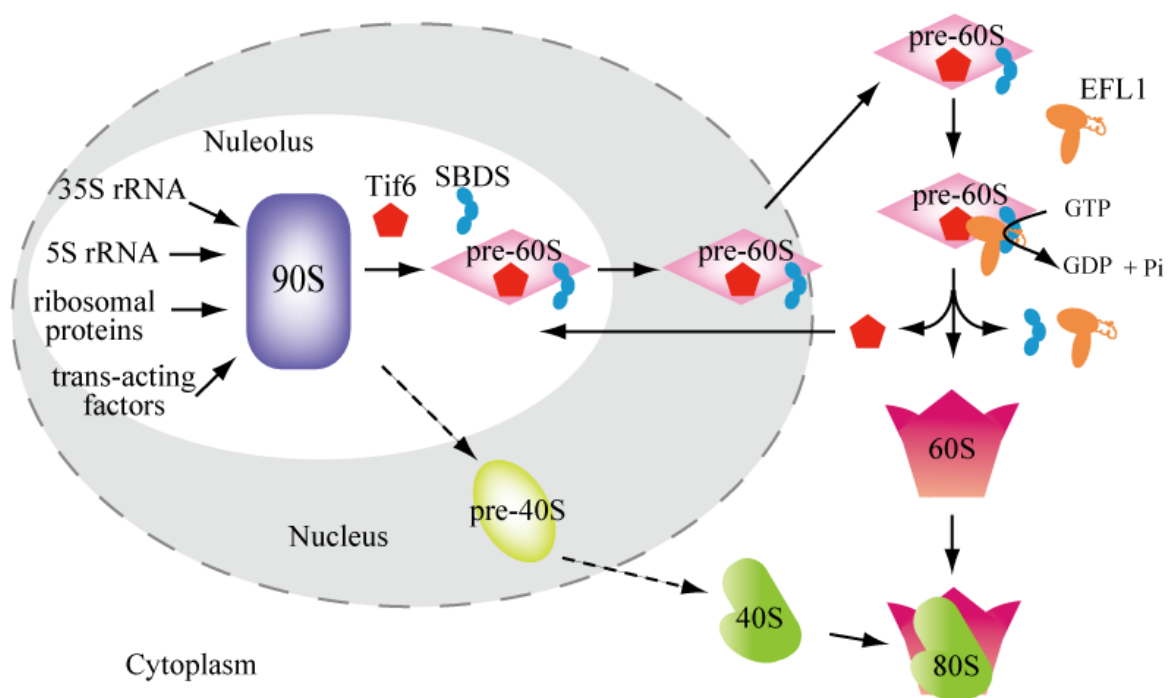


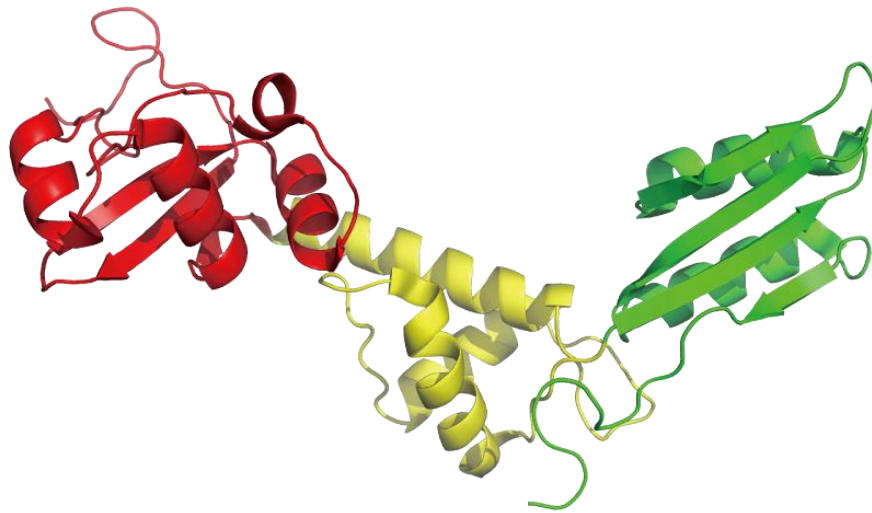
Fig. 2-1 Overview of ribosome biogenesis related to releasing to Tif6.

1.2 SBDS and EFL1

Shwachman-Diamond syndrome is an autosomal recessive disorder characterized by hematological dysfunction, pancreatic exocrine insufficiency, skeletal abnormalities, and short stature (53). Approximately 90% of Shwachman–Diamond syndrome cases are caused by mutations in the Shwachman–Bodian–Diamond syndrome (SBDS) gene (54), which encodes a protein of approximately 250 amino acid residues. Orthologs of SBDS have been found in archaea, plants, and other eukaryotes. SBDS is composed of three domains (Fig. 2-2), and missense mutations of SBDS associated with Shwachman-Diamond syndrome were identified in all three domains (50). Nuclear magnetic resonance (NMR) spectroscopy identified domain I of SBDS as an RNA binding site (55). Moreover, it was reported that two mutants in domain II (R126T and K151N in human) were defective in triggering Tif6 release (52). However, the roles of domains II and III were unclear.

On the other hand, EFL1 shares 26.8% sequence identity with translation elongation factor 2 (EF2), and these two proteins share a ribosome binding site (56). EFL1 triggers release of Tif6 from the pre-60S ribosome, whereas EF2 assists in the translocation of tRNA and mRNA from the A-site to the P-site of the ribosome. There is a marked difference in domain composition between these proteins, i.e., insertion of an extra ~150-residue domain in EFL1. EFL1 and EF2 are commonly composed of domains G, G', and II – V, but only EFL1 has the insertion region within domain II (Fig. 2-3) (57). Although the insertion domain is expected to be an important determinant of the function, the details are still unclear.

Here, I performed interaction analysis of EFL1 and SBDS. The results showed that EFL1 binds directly with SBDS, in which the insertion region of EFL1 and domain II – III of SBDS dominate the interaction. The results of spectroscopic analysis taken together with the thermodynamic properties suggested conformational changes in the insertion region of EFL1 coupled with the interaction. Based on these observations, I discuss the significance of the interaction between EFL1 and SBDS for Tif6 removal.



HsSBDS

I	II	III
S2	D97 S96	A170 H171 E250

Fig. 2-2 Structure of Human SBDS. PDB code; 2L9N

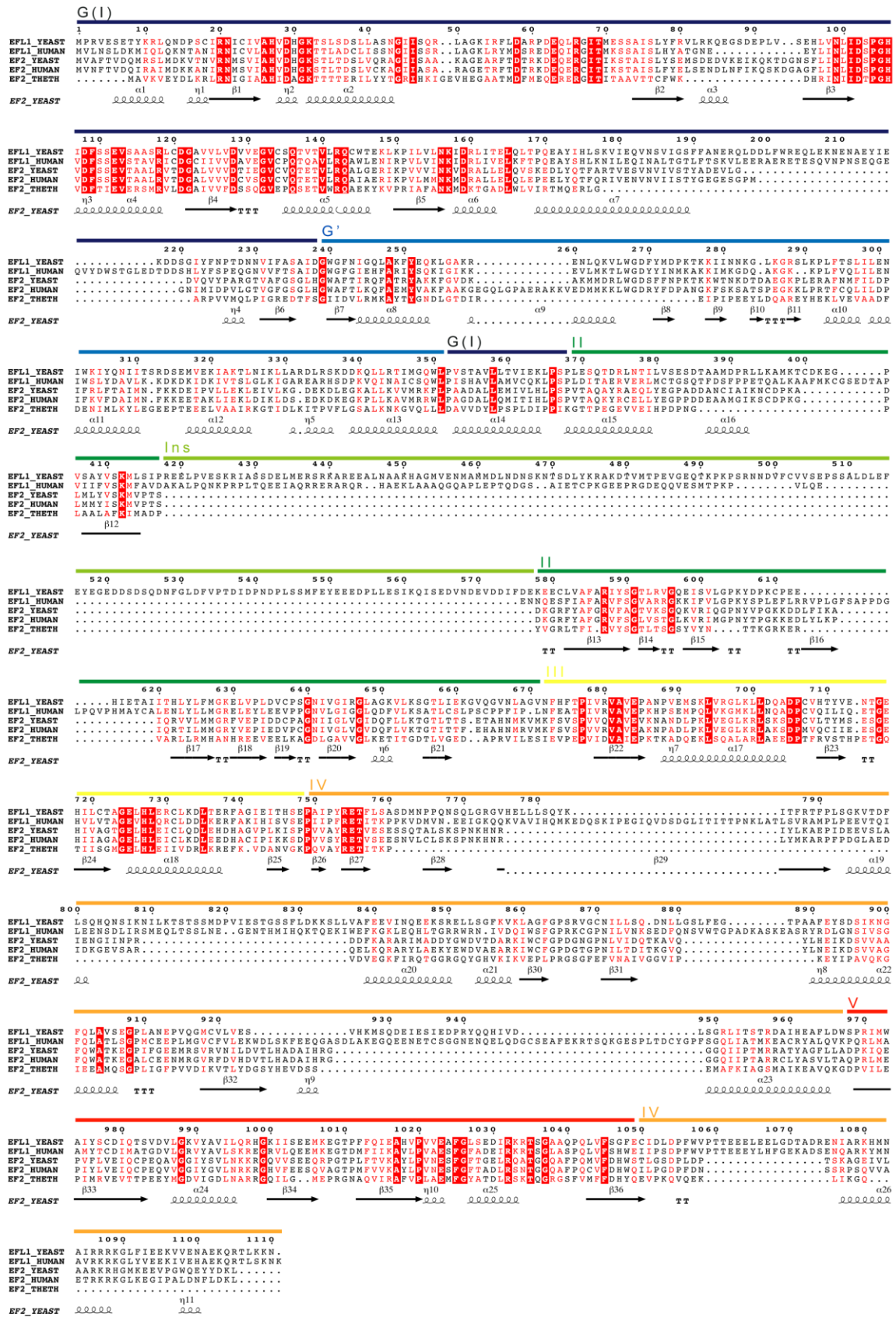


Fig. 2-3 Amino acid sequence alignment of EFL1 and EF2. Domains are represented by color bars above. Secondary structure elements of *S. cerevisiae* EF2 are also shown.

2 Material and methods

2.1 Plasmid construction

The gene encoding EFL1 was amplified by PCR from *S. cerevisiae* genomic DNA using the primers EFL1-S-1 and EFL1-AS-1 (Table 2-1), and inserted into the SbfI–AscI sites of a modified pET26b vector (pECO-H2). In the resultant plasmid, a His-tag was attached to the N-terminus of the EFL1 gene. The plasmid for EFL1- Δ Ins (deletion mutant of the insertion region encoding residues 418 – 577) was constructed by the inverse PCR method using the EFL1 expression vector as the template and primers EFL1-S-2 and EFL1-AS-2. The DNA fragment for the insertion domain of EFL1 (EFL1-Ins; encoding residues 419 – 577) was amplified using the primers EFL1-S3 and EFL1-AS-3, followed by insertion into the SbfI–AscI sites of a modified pET26b vector (pECO-GH1). In the resultant plasmid, a GST-tag followed by a TEV protease site and a His-tag were fused at the N-terminus and C-terminus, respectively.

The gene encoding SBDS was amplified by PCR from *S. cerevisiae* genomic DNA using the primers SBDS-S-4 and SBDS-AS-4, and inserted into the NdeI–XhoI sites of a modified pET28b vector (pDBHT-2), in which a His-tag was fused at the N-terminus. The coding sequences of SBDS domain I (encoding residues 1 – 94), domain II (encoding residues 95 – 172), domain III (encoding residues 173 – 250), domain I – II (encoding residues 1 – 172), and domain II – III (encoding residues 95 – 250) were amplified separately by PCR with the expression vector of SBDS as the template and the primers shown in Supplementary Table 1 and 2. The amplified DNA fragments encoding domains I, II, and I – II were inserted into the NdeI–XhoI sites of a modified pET28b vector (pET28M), in which His-tag was fused at the N-terminus. The DNA fragments encoding domain III and II – III were inserted into the NdeI–XhoI sites of the pET26b vector, in which His-tag was attached to the C-terminus.

Table 2-1 Plasmids

Name	Vector	Construct	Primers
EFL1	pECO-H2	His tag at N-terminus	S-1, AS-1
EFL1ΔIns	pECO-H2	His tag at N-terminus	S-2, AS-2
EFL1-Ins	pECO-GH1	GST tag – TEV protease site at N-terminus, His tag at C-terminus	S-3, AS-3
SBDS	pDBHT-2	His tag at N-terminus	S-4, AS-4
SBDS domain I	pET28M	His tag at N-terminus	S-4, AS-5
SBDS domain II	pET28M	His tag at N-terminus	S-5, AS-6
SBDS domain III	pET26M	His tag at C-terminus	S-6, AS-4
SBDS domain I – II	pET28M	His tag at N-terminus	S-4, AS-6
SBDS domain II – III	pET26M	His tag at C-terminus	S-5, AS-4

Table 2-2 Primers used in this study

Name	Sequence
S-1	CCC ACC TGC AGG GTG GTA GCA TGC CTA GAG TGG AAT CG
S-2	CAA TTC CTA AGG AAG AAT GCT TGG TAG CAT
S-3	CCC ACC TGC AGG GTG GTA GCA TGG AAG AAT TAC CTG TTG AAT CTA AGA G
S-4	TGG TGC CGC GCG GCA GCC ATA TGC CTA TCA ATC AAC CGT
S-5	GGA ATT CCA TAT GCA ATT ATC GGA AAA AGA AAG ACA ATT AAT G
S-6	GGA ATT CCA TAT GGC GAA GAT GAA AGT CAA AGT G
AS-1	GGG TGG CGC GCC TTA ATT CTT TTT CAA AGT ACG TTG TTT TT
AS-2	TCT TCC TTA GGA ATT GAA AGC ATC TTA GAT
AS-3	GGG TGG CGC GCC TTC GTC AAA AAT ATC ATC TAC TTC ATC GTT C
AS-4	TGG TGG TGG TGG TGC TCG AGT TAG TTA TGC GTT GTA TTA TCT ATG AC
AS-5	CCG CTC GAG TTA TTG AAT CTC TCC CTT ATG CAT GA
AS-6	CCG CTC GAG TTA CGC CCT TAC TAT TGG AAT AAT TTG

2.2 Protein expression and purification

Escherichia coli strain B834 (DE3) harboring the expression vector and pRARE2 was grown at 37°C in LB medium supplemented with 25 µg/mL kanamycin and 34 µg/mL chloramphenicol until the OD₆₀₀ reached 0.6. To induce expression of the desired protein, IPTG was added at a final concentration of 0.25 mM. After incubation at 25°C for a further 18 h (exceptionally, for the expression of EFL1, 15°C for 24 h), cells were harvested by centrifugation at 4500 × g for 10 min at 4°C. Cells expressing EFL1 and the mutants were resuspended in 50 mM Tris-HCl (pH 7.5), 300 mM NaCl, 1 mM MgCl₂, 10% (v/v) glycerol, 1 mg/mL lysozyme, and 0.1 mg/mL DNase I. Cells expressing SBDS and the mutants were resuspended in 50 mM Tris-HCl (pH 7.5), 300 mM NaCl, 10% (v/v) glycerol, 1 mg/mL lysozyme, 0.1 mg/mL DNase I, and 0.1 mg/mL RNase A. Resuspended cells were disrupted by sonication, followed by centrifugation at 40000 × g for 1 h at 10°C.

EFL1 and EFL1-ΔIns were purified on a HisTrap HP column (GE Healthcare) and HiLoad 16/60 Superdex 200-pg column (GE Healthcare). EFL1-Ins was purified on a HisTrap HP column (GE Healthcare), followed by removal of the GST-tag by digestion with TEV protease. EFL1-Ins without the GST-tag was further purified on a HisTrap HP column and HiLoad 16/60 Superdex 200-pg column.

SBDS and its truncated mutants were purified on a HisTrap HP column and HiLoad 26/60 Superdex 75-pg column. Exceptionally, SBDS-domain I was purified by three steps using a HisTrap HP column, HiTrap Heparin HP column, and HiLoad 26/60 Superdex 75-pg column.

2.3 Gel filtration analyses

Aliquots of 150 µL consisting of 2.5 nmol EFL1 and 8.5 nmol SBDS were loaded onto a HiLoad 10/300 Superdex 200-pg column (GE Healthcare) pre-equilibrated with 20 mM Tris-HCl (pH 7.5), 150 mM NaCl, 1mM MgCl₂, 5% (v/v) glycerol, and 5 mM β-mercaptoethanol. Control experiments using each protein were also performed under the same conditions. Peak fractions were analyzed by SDS-PAGE, followed by staining with Coomassie brilliant blue R-250.

2.5 Gel shift assay

Gel shift assay was performed in 5- μ L reaction mixtures containing 20 mM Tris-HCl (pH 7.5), 150 mM NaCl, 1 mM MgCl₂, 5% (v/v) glycerol, 5 mM β -mercaptoethanol, and the desired amounts of EFL1 and SBDS. Reaction mixtures were loaded onto a 3% – 10% native gradient polyacrylamide gel (PAGEL NPG-310L; ATTO). Electrophoresis conditions were as follows: temperature, 4°C; power voltage, 100 V; and electrophoresis buffer, 50 mM Tris-MES (pH 8.0) and 10 mM Mg (OAc)₂. Proteins were visualized using SYPRO® Ruby Protein gel stain.

2.6 Isothermal titration calorimetry

All isothermal titration calorimetry (ITC) measurements were carried out with a VP-ITC System (MicroCal). Proteins were dialyzed against a buffer containing 20 mM Tris-HCl (pH 7.5), 150 mM NaCl, 1 mM MgCl₂, 10% (v/v) glycerol, and 5 mM β -mercaptoethanol at 4°C. All measurements were conducted at 30°C and protein solutions were degassed under vacuum prior to use. The cell was filled with ~5 μ M full-length EFL1, EFL1- Δ Ins or ~2.5 μ M EFL1-Ins, and a syringe was filled with ~50 μ M full-length SBDS or each truncated SBDS. The solution of SBDS was injected 25 times in portions of 10 μ L over 20 s. The data were analyzed using the program ORIGIN (MicroCal).

2.7 Circular dichroism measurements

Circular dichroism (CD) spectra were measured on a JASCO J-720 spectropolarimeter (JASCO) in a quartz cell with an optical path length of 2 mm. The CD spectra were obtained by taking the average of four scans made from 300 to 190 nm and normalized to molar ellipticities by protein concentrations.

2.8 Model building of EFL1-Tif6-bound ribosome

The binding position of Tif6 on EF2-60S complex was obtained by superposing 60S ribosome subunits of eIF6 (Tif6)-60S (PDB code: 4A18 (58)) and EF2-60S complex structure (PDB code: 1S1H and 1S1I (59)) using the program PyMoL(34). The final model of the EFL1-Tif6-bound 60S ribosome subunit was built by superposing the crystal structure of Tif6 (PDB code: 1G62 (48)) onto the Tif6-EF2-60S model (60).

3 Results

3.1 Interaction between EFL1 and SBDS

To investigate the details of the interaction between EFL1 and SBDS, the binding of EFL1 with SBDS was analyzed by size exclusion chromatography (SEC), gel shift assay, and isothermal titration calorimetry (ITC). Figure 2-4A shows the results of SEC. Compared with EFL1 and SBDS eluted with peaks at 11.19 mL and 15.15 mL, respectively, the mixture showed a slightly earlier peak at 11.11 mL. SDS-PAGE showed that both EFL1 and SBDS were contained in the peak of mixed sample (Fig. 2-4B), indicating the direct interaction between EFL1 and SBDS. Gel shift assay also clearly showed the interaction between EFL1 and SBDS (Fig. 2-4C). With increasing concentration of SBDS, the migration speed of EFL1 was significantly slowed. As EFL1 has GTPase activity, these experiments were also performed in the presence of GDPNP (an analog of GTP). However, there were no significant differences from the results in the absence of GTP (Fig. 2-4A). These results indicated that EFL1 and SBDS directly interact with each other in a GTP-independent manner. Next, I determined the thermodynamic parameters of the interaction by ITC (Fig. 2-4D and Table 2-3). The association constant and stoichiometry were $12.7 \times 10^6 \text{ M}^{-1}$ and 0.94, respectively, indicating that EFL1 binds to SBDS with a molar ratio of 1:1. The binding enthalpy, entropy, and Gibbs's energy were calculated to be $-14.0 \text{ kcal mol}^{-1}$, $-13.5 \text{ cal mol}^{-1} \text{ K}^{-1}$, and $-9.86 \text{ kcal mol}^{-1}$, respectively, indicating that the interaction between EFL1 and SBDS is driven by enthalpy and is entropically disadvantageous.

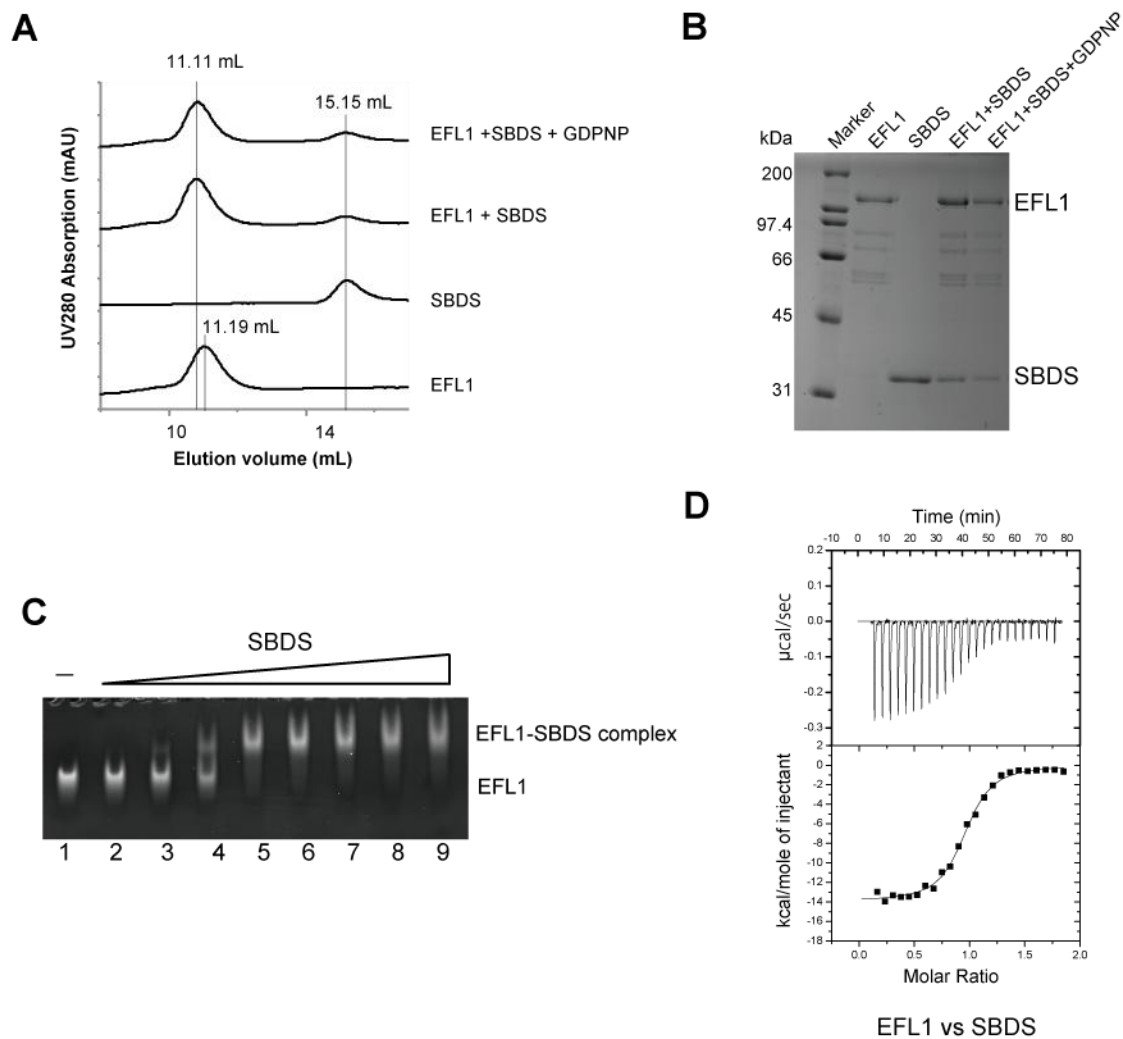


Fig. 4 Interaction between EFL1 and SBDS. (A) Size exclusion chromatography of EFL1 incubated with SBDS. Chromatograms of EFL1, SBDS, and their complex in the presence of GDPNP are also shown. The elution volumes are indicated at the tops of the peaks. (B) SDS-PAGE of the peak fractions on size exclusion chromatography. Lane 1, EFL1; lane 2, SBDS; lane 3, EFL1-SBDS; lane 4, EFL1-SBDS in the presence of GDPNP. (C) Results of gel shift assay. A 50-pmol aliquot of EFL1 was incubated with different amounts of SBDS. Lane 1, EFL1 only; lanes 2 – 8, increasing amounts of SBDS (2, 5, 10, 25, 50, 100, 500, 1000 pmol). (D) Thermogram of interaction between EFL1 and SBDS.

Table 2-3. Affinity and thermodynamic parameters of binding between SBDS and EFL1 at 30°C

EFL1	SBDS	N	K_b ($\times 10^6 M^{-1}$)	K_d^a (nM)	ΔH (kcal·mol ⁻¹)	ΔS (cal·mol ⁻¹ ·K ⁻¹)	ΔG^b (kcal·mol ⁻¹)
full length	full length	0.94 ± 0.007	12.7 ± 1.51	78.7	-14.0 ± 0.17	-13.5	9.86

^a $K_d = 1/K_b$

^b $\Delta G = -RT \ln K_b = \Delta H - T\Delta S$

3.2 Identification of the binding region in EFL1

EFL1 shares sequence similarity with translation elongation factors, EF-G and EF-2 (Fig. 2-5A and Fig. 2-3). These proteins commonly consist of the G domain (domain I), which binds with and hydrolyzes GTP, the G' domain, and domains II to V (Fig. 2-3). On the other hand, EFL1 has a characteristic insertion domain of 160 amino acids within domain II. To clarify the contribution of the insertion domain to the interaction with SBDS, the insertion domain of EFL1 (EFL1-Ins; Gly419-Glu577) and a mutant protein in which the insertion domain was deleted (EFL1- Δ Ins) were prepared, and their affinities with SBDS were evaluated by ITC (Fig. 2-5B). EFL1-Ins bound with SBDS, whereas no significant interaction was observed for EFL1- Δ Ins. The association constant, $11.8 \times 10^6 \text{ M}^{-1}$ of EFL1-Ins, did not decrease markedly compared with that of EFL1 (Table 2-4). The thermodynamic parameters were binding enthalpy of $-16.7 \text{ kcal mol}^{-1}$ and binding entropy of $-22.8 \text{ cal mol}^{-1} \text{ K}^{-1}$, indicating that EFL1-Ins binds to SBDS in an enthalpy-driven manner, which was the same as that of EFL1. Furthermore, EFL1 and EFL1 Δ Ins showed similar circular dichroism (CD) spectra, suggesting that truncation of the insertion domain did not affect the folding of EFL1 (Fig. 2-6). These observations indicated that the insertion region of EFL1 plays a pivotal role in the interaction with SBDS. The CD spectrum of EFL1-Ins showed a weak negative peak around 220 nm and strong negative CD around 200 nm (Fig. 2-6). These spectral features indicated that the insertion domain has a random structure with a small quantity of β -strands.

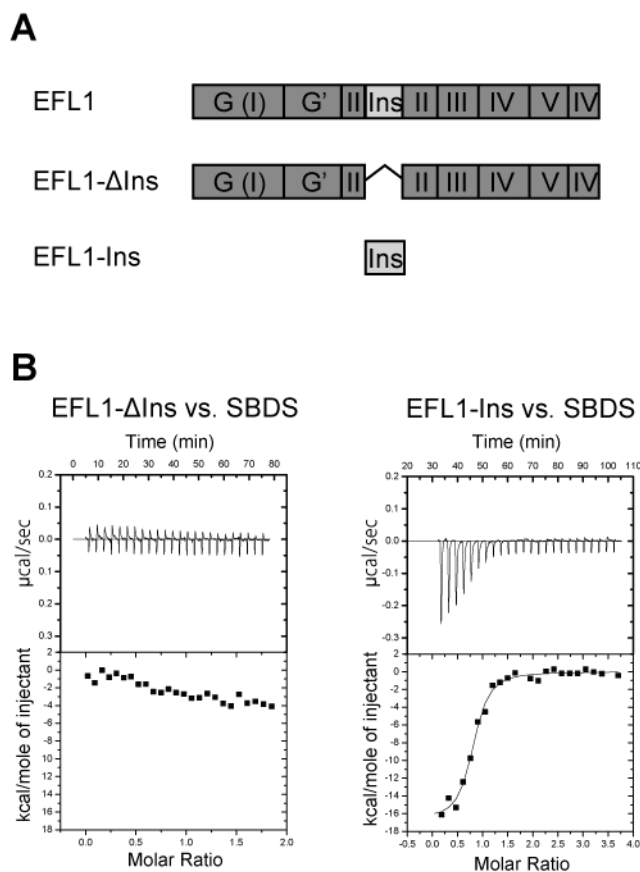


Fig. 2-5 Interaction of EFL1 mutants for SBDS. (A) Schematic overview of the EFL1 variants. The insertion sequence within domain II is shown in light gray. (B) Thermograms of titration for SBDS of EFL1-ΔIns (left) and EFL1-Ins (right).

Table 2-4. Affinities and thermodynamic parameters of binding between SBDS and EFL1 mutants at 30°C

EFL1	SBDS	N	K_b ($\times 10^6 M^{-1}$)	K_d (nM)	ΔH (kcal·mol ⁻¹)	ΔS (cal·mol ⁻¹ ·K ⁻¹)	ΔG (kcal·mol ⁻¹)
ΔIns	full length	ND ^a	ND	ND	ND	ND	ND
Ins	full length	0.778 ± 0.02	11.8 ± 2.45	84.7	-16.7 ± 0.51	-22.8	9.81

^aND: not detected.

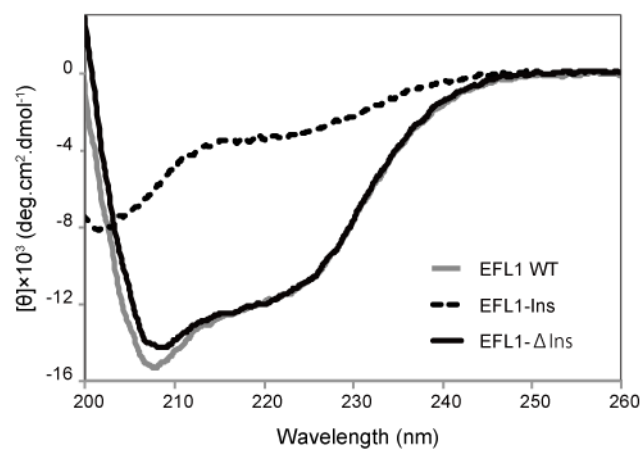


Fig. 2-6 CD spectra of EFL1 variants. Gray line; EFL1 wild type, black line; EFL1- Δ Ins, dotted black line; EFL1-Ins.

3.3 Identification of the binding region in SBDS

It has been reported that SBDS is composed of three domains with weak contacts among them (50,52,55). As SBDS family proteins share a similar structure and sequence, ScSBDS is expected to consist of domain I (Met1 – Gln94), domain II (Leu95 – Ala172), and domain III (Lys173 – Asn250) (Fig. 2-2). Therefore, I prepared five domain-truncated mutants of SBDS (SBDS I, SBDS II, SBDS III, SBDS I – II, and SBDS II – III), and their interactions with EFL1 were evaluated by ITC (Fig. 2-7 and Table 2-5).

SBDS II – III showed significant interaction with EFL1, whereas domain I – II did not (Fig. 2-7A and B). The association constant of SBDS II – III with EFL1 was determined to $1.19 \times 10^6 \text{ M}^{-1}$. The thermodynamic parameters indicated an enthalpy-driven and entropically disadvantageous interaction as observed in the interaction between intact SBDS and EFL1. Despite the observations in SBDS II – III, none of the other SBDS mutants showed significant interactions with EFL1 by themselves. These results indicated that both domains II and III of SBDS contribute to the interaction with EFL1. Taken together, these results indicated that the insertion domain of EFL1 and both domains II and III of SBDS dominate the enthalpy-driven entropically disadvantageous interaction between EFL1 and SBDS.

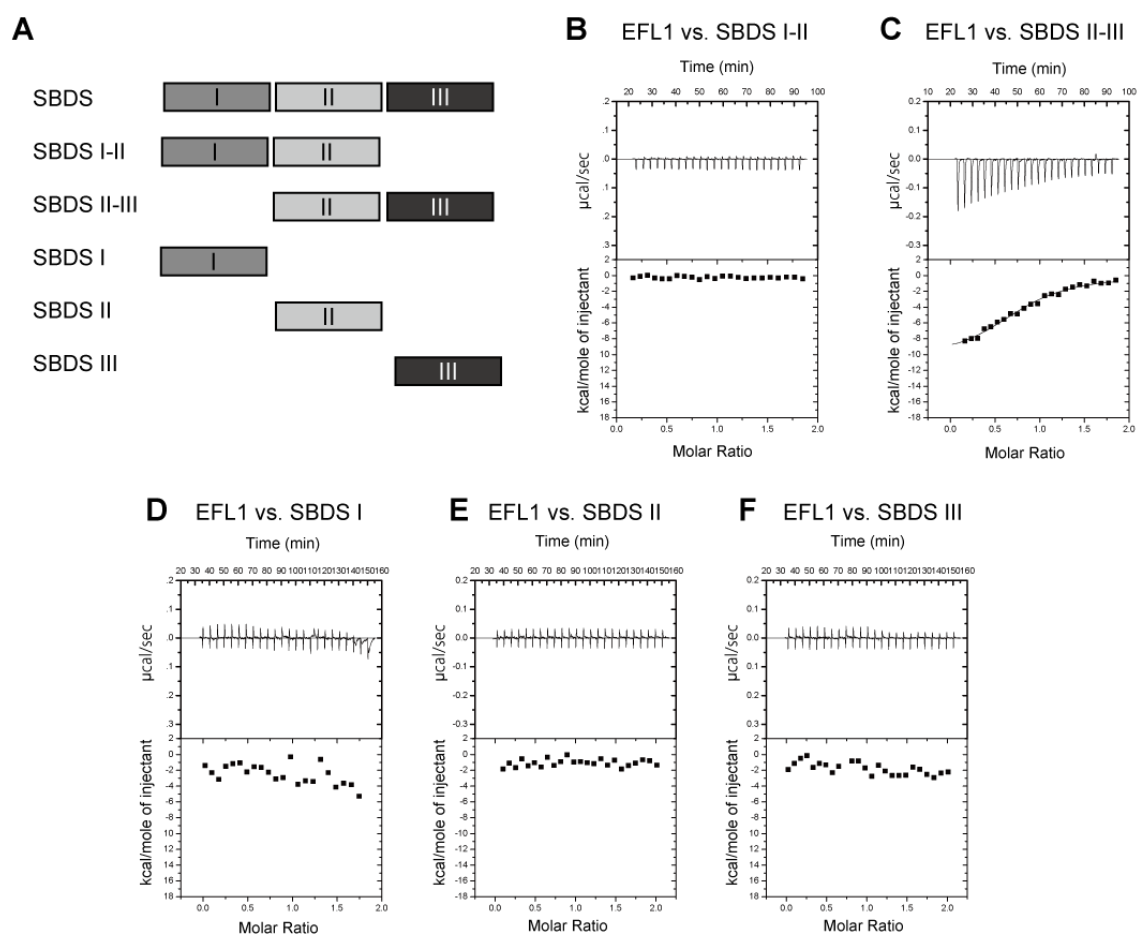


Fig. 2-4 Interaction of SBDS mutants for EFL1. (A) Schematic overview of the SBDS variants. (B – F) Thermograms of titration of SBDS variants for EFL1. B; SBDS I – II, C; SBDS II – III, D; SBDS I, E; SBDS II, F; SBDS III.

Table 2-5. Affinities and thermodynamic parameters of binding between SBDS mutants and EFL1 at 30°C

EFL1	SBDS	N	K_b ($\times 10^6 \text{M}^{-1}$)	K_d (nM)	ΔH ($\text{kcal}\cdot\text{mol}^{-1}$)	ΔS ($\text{cal}\cdot\text{mol}^{-1}\cdot\text{K}^{-1}$)	ΔG ($\text{kcal}\cdot\text{mol}^{-1}$)
full length	I – II	ND	ND	ND	ND	ND	ND
full length	II – III	0.803 ± 0.03	1.19 ± 1.69	840	-10.6 ± 0.52	-7.04	8.43
full length	I	ND	ND	ND	ND	ND	ND
full length	II	ND	ND	ND	ND	ND	ND
full length	III	ND	ND	ND	ND	ND	ND

^a ND: not detected.

4 Discussion

4.1 Biological implications of SBDS – EFL1 interaction

Both SBDS and EFL1 were bound with the ribosome by itself (52). It has been reported that EFL1 binds at the same site on the ribosome as EF2 (56), whereas the site for SBDS binding has not yet been identified. Our results showed that EFL1 interacted with SBDS directly, and this is the first study demonstrating the detailed interaction between them. The direct interaction indicated that SBDS binds in the vicinity of the EF2/EFL1 binding site on the ribosome. Oliveira et al. demonstrated that SBDS interacted with ribosomal RNA via domain I (55). In addition, Finch et al. showed that the motion of domain I of SBDS was independent of domain II – III (52). Our results demonstrated a significant role of domain II – III of SBDS in the interaction with EFL1. Taken together, these results suggest that domains I and II – III of SBDS are likely to act as functionally independent domains; i.e., domain I and domain II – III bind to the ribosome and EFL1, respectively. EFL1 competes with EF2 for binding at the ribosomal GTPase binding site. This site will be occupied by EFL1 during ribosome biogenesis, whereas EF2 binds there in the elongation step during translation. The interaction between SBDS and EFL1 may facilitate predominant recruitment of EFL1 in the final maturation process of ribosome biogenesis.

To discuss the significance of the SBDS – EFL1 interaction in release of Tif6, a structural model of Tif6-EFL1-60S complex was constructed from the crystal structures of Tif6-60S complex and EF2-60S complex (Fig. 2-8). In the model, EFL1 is positioned adjacent to Tif6, in which domain II of EFL1 is expected to show extensive interactions with Tif6. The insertion domain of EFL1, which is located within domain II, is necessary for the interaction with SBDS. Therefore, the insertion domain is likely to be toward Tif6. As the insertion domain is recognized by SBDS, the binding site of SBDS on the ribosome is expected to be close to the Tif6 binding site. Taken together, it is plausible that both EFL1 and SBDS are positioned in close proximity to Tif6 on the ribosome. However, the results of size exclusion chromatography indicated that Tif6 interacts with neither EFL1 nor SBDS directly (Fig. 2-9). Biochemical analyses demonstrated that the presence of both EFL1 and SBDS, and GTP hydrolysis of EFL1 are all essential for the release of Tif6. Moreover, the presence of SBDS enhances the GTPase activity of EFL1 (52,61). SBDS may increase the GTPase activity of EFL1 through complex formation. This is supported by the report that substitution in the domain II – III of SBDS resulted in a significant decrease in GTPase

activity of EFL1 (52). The GTPase activity would induce a conformational change of EFL1 as observed from other translational factors possessing GTPase activity, e.g., EF2 (57,62). As Tif6 did not interact with EFL1 directly (Fig. 2-8), the conformational change of EFL1 is likely to trigger release of Tif6 indirectly. As reported for EF2, the conformational change of EFL1 may induce rearrangement of the ribosome, which may result in the release of Tif6. These are consistent with the mechanism proposed previously (51).

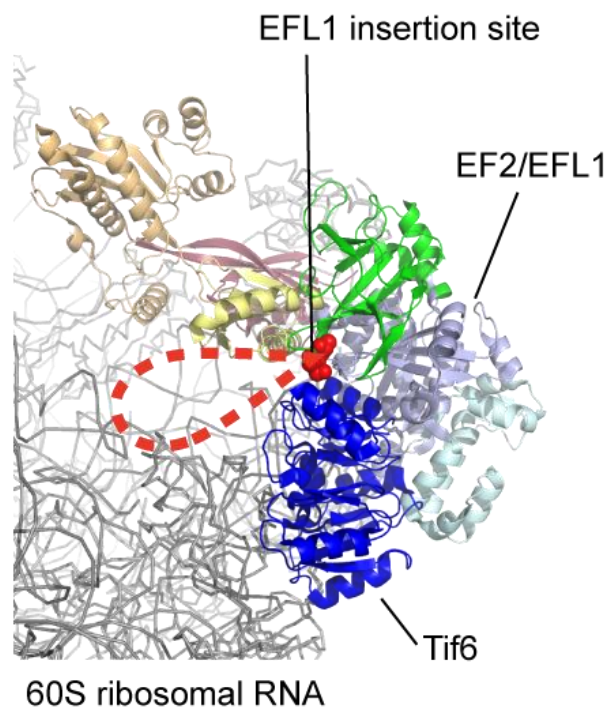


Fig. 2-8 Structure model of ribosome-Tif6-EFL1/EF2 ternary complex. Red spheres represent the site in which the insertion domain is located. Tif6 and EF2 are colored as follows. blue, Tif6; light brown, domain IV of EF2/EFL1; yellow, domain III of EF2/EFL1; pink, V of EF2/EFL1; green, domain II of EF2/EFL1; purple, domain G(I) of EF2/EFL1; cyan, domain G' of EFL1/EF2; gray, ribosomal RNA.

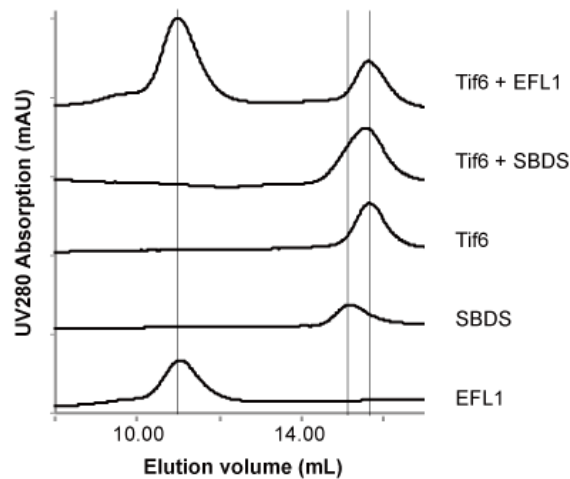


Fig. 2-9 Size exclusion chromatography of Tif6 incubated with EFL1 and SBDS. Chromatograms of Tif6, EFL1, and SBDS are also shown.

4.2 Role of the insertion domain of EFL1

Although EFL1 and EF2 bind to the identical site on the ribosome, they have different functions (56). They are clearly distinguished each other by the presence or absence of an insertion sequence within domain II. The CD spectra showed that the insertion domain of EFL1 (EFL1-Ins) was a random structure. On the other hand, ITC experiments showed that the interaction between EFL1 and SBDS was entropically disadvantageous. These observations indicate that the random structure of the insertion domain of EFL1 became static upon SBDS binding. It is likely that the insertion domain acts as an intrinsically disordered protein. Similar structural transition from a flexible to a rigid form coupled with ligand binding was reported previously for initiation factors (63). The GTPase activity of EFL1 necessary for Tif6 release is enhanced by the presence of SBDS (52). Our results indicated a direct interaction of the insertion domain of EFL1 with SBDS accompanying conformational transition. These observations suggest that the fixed conformation is important for the release of Tif6. EFL1 may be necessary to acquire the intrinsically disordered domain as an insertion domain to express these two different functions, i.e., inhibition of EF2-like activity utilizing the unfolded structure and promoting Tif6 release in the fixed form.

Reference

1. Ben-Shem, A., Jenner, L., Yusupova, G. and Yusupov, M. (2010) Crystal structure of the eukaryotic ribosome. *Science*, **330**, 1203-1209.
2. Ben-Shem, A., Garreau de Loubresse, N., Melnikov, S., Jenner, L., Yusupova, G. and Yusupov, M. (2011) The structure of the eukaryotic ribosome at 3.0 Å resolution. *Science*, **334**, 1524-1529.
3. Venema, J. and Tollervey, D. (1999) Ribosome synthesis in *Saccharomyces cerevisiae*. *Annu Rev Genet*, **33**, 261-311.
4. Kressler, D., Linder, P. and de La Cruz, J. (1999) Protein trans-acting factors involved in ribosome biogenesis in *Saccharomyces cerevisiae*. *Mol Cell Biol*, **19**, 7897-7912.
5. Tschochner, H. and Hurt, E. (2003) Pre-ribosomes on the road from the nucleolus to the cytoplasm. *Trends Cell Biol*, **13**, 255-263.
6. Gadai, O., Strauss, D., Petfalski, E., Gleizes, P.E., Gas, N., Tollervey, D. and Hurt, E. (2002) Rlp7p is associated with 60S preribosomes, restricted to the granular component of the nucleolus, and required for pre-rRNA processing. *J Cell Biol*, **157**, 941-951.
7. Joseph, N., Krauskopf, E., Vera, M.I. and Michot, B. (1999) Ribosomal internal transcribed spacer 2 (ITS2) exhibits a common core of secondary structure in vertebrates and yeast. *Nucleic Acids Res*, **27**, 4533-4540.
8. Yeh, L.C. and Lee, J.C. (1990) Structural analysis of the internal transcribed spacer 2 of the precursor ribosomal RNA from *Saccharomyces cerevisiae*. *J Mol Biol*, **211**, 699-712.
9. Woolford, J.L., Jr. and Baserga, S.J. (2013) Ribosome biogenesis in the yeast *Saccharomyces cerevisiae*. *Genetics*, **195**, 643-681.
10. Zhang, J., Harnpicharnchai, P., Jakovljevic, J., Tang, L., Guo, Y., Oeffinger, M., Rout, M.P., Hiley, S.L., Hughes, T. and Woolford, J.L., Jr. (2007) Assembly factors Rpf2 and Rrs1 recruit 5S rRNA and ribosomal proteins rpL5 and rpL11 into nascent ribosomes. *Genes Dev*, **21**, 2580-2592.
11. Wehner, K.A. and Baserga, S.J. (2002) The sigma(70)-like motif: a eukaryotic RNA binding domain unique to a superfamily of proteins required for ribosome biogenesis. *Mol Cell*, **9**, 329-339.
12. Morita, D., Miyoshi, K., Matsui, Y., Toh, E.A., Shinkawa, H., Miyakawa, T. and Mizuta, K. (2002) Rpf2p, an evolutionarily conserved protein, interacts with ribosomal protein L11 and is essential for the processing of 27 SB Pre-rRNA to 25 S rRNA and the 60 S ribosomal subunit assembly in *Saccharomyces cerevisiae*. *J Biol Chem*, **277**, 28780-28786.
13. Miyoshi, K., Tsujii, R., Yoshida, H., Maki, Y., Wada, A., Matsui, Y., Toh, E.A. and Mizuta, K. (2002) Normal assembly of 60 S ribosomal subunits is required for the signaling in response to a secretory defect in *Saccharomyces cerevisiae*. *J Biol Chem*, **277**, 18334-18339.
14. Miyoshi, K., Shirai, C., Horigome, C., Takenami, K., Kawasaki, J. and Mizuta, K. (2004) Rrs1p, a ribosomal protein L11-binding protein, is required for nuclear export of the 60S pre-ribosomal subunit in *Saccharomyces cerevisiae*. *FEBS Lett*, **565**, 106-110.
15. Nariai, M., Tanaka, T., Okada, T., Shirai, C., Horigome, C. and Mizuta, K. (2005) Synergistic defect in 60S ribosomal subunit assembly caused by a mutation of Rrs1p, a ribosomal protein L11-binding protein, and 3'-extension of 5S rRNA in *Saccharomyces cerevisiae*. *Nucleic Acids Res*, **33**, 4553-4562.
16. Eisenhaber, F., Wechselberger, C. and Kreil, G. (2001) The Brix domain protein family -- a key to the ribosomal biogenesis pathway? *Trends Biochem Sci*, **26**, 345-347.
17. Lee, S.J. and Baserga, S.J. (1999) Imp3p and Imp4p, two specific components of the U3 small nucleolar ribonucleoprotein that are essential for pre-18S rRNA processing. *Mol Cell Biol*, **19**, 5441-5452.
18. Granneman, S., Gallagher, J.E., Vogelzangs, J., Horstman, W., van Venrooij, W.J., Baserga, S.J. and Pruijn, G.J. (2003) The human Imp3 and Imp4 proteins form a ternary complex with hMpp10, which only interacts with the U3 snoRNA in 60-80S ribonucleoprotein complexes. *Nucleic Acids Res*, **31**, 1877-1887.

19. Hsieh, Y.C., Tu, P.J., Lee, Y.Y., Kuo, C.C., Lin, Y.C., Wu, C.F. and Lin, J.J. (2007) The U3 small nucleolar ribonucleoprotein component Imp4p is a telomeric DNA-binding protein. *Biochem J*, **408**, 387-393.
20. Ng, C.L., Waterman, D., Koonin, E.V., Antson, A.A. and Ortiz-Lombardia, M. (2005) Crystal structure of Mil (Mth680): internal duplication and similarity between the Imp4/Brix domain and the anticodon-binding domain of class IIa aminoacyl-tRNA synthetases. *EMBO Rep*, **6**, 140-146.
21. Tsuno, A., Miyoshi, K., Tsujii, R., Miyakawa, T. and Mizuta, K. (2000) RRS1, a conserved essential gene, encodes a novel regulatory protein required for ribosome biogenesis in *Saccharomyces cerevisiae*. *Mol Cell Biol*, **20**, 2066-2074.
22. Horigome, C., Okada, T., Shimazu, K., Gasser, S.M. and Mizuta, K. (2011) Ribosome biogenesis factors bind a nuclear envelope SUN domain protein to cluster yeast telomeres. *EMBO J*, **30**, 3799-3811.
23. Yao, K., You, X., Shi, L., Wan, W., Yu, F. and Chen, J. (2008) Two-dimensional molecular space with regular molecular structure. *Langmuir*, **24**, 302-309.
24. Kabsch, W. (2010) Xds. *Acta Crystallogr D Biol Crystallogr*, **66**, 125-132.
25. Matthews, B.W. (1968) Solvent content of protein crystals. *J Mol Biol*, **33**, 491-497.
26. Terwilliger, T.C., Adams, P.D., Read, R.J., McCoy, A.J., Moriarty, N.W., Grosse-Kunstleve, R.W., Afonine, P.V., Zwart, P.H. and Hung, L.W. (2009) Decision-making in structure solution using Bayesian estimates of map quality: the PHENIX AutoSol wizard. *Acta Crystallogr D Biol Crystallogr*, **65**, 582-601.
27. McGuffin, L.J., Bryson, K. and Jones, D.T. (2000) The PSIPRED protein structure prediction server. *Bioinformatics*, **16**, 404-405.
28. Ward, J.J., McGuffin, L.J., Bryson, K., Buxton, B.F. and Jones, D.T. (2004) The DISOPRED server for the prediction of protein disorder. *Bioinformatics*, **20**, 2138-2139.
29. Asano, N., Nakamura, A., Komoda, K., Kato, K., Tanaka, I. and Yao, M. (2014) Crystallization and preliminary X-ray crystallographic analysis of ribosome assembly factors: the Rpf2-Rrs1 complex. *Acta Crystallogr F Struct Biol Commun*, **70**, 1649-1652.
30. Terwilliger, T.C., Grosse-Kunstleve, R.W., Afonine, P.V., Moriarty, N.W., Zwart, P.H., Hung, L.W., Read, R.J. and Adams, P.D. (2008) Iterative model building, structure refinement and density modification with the PHENIX AutoBuild wizard. *Acta Crystallogr D Biol Crystallogr*, **64**, 61-69.
31. McCoy, A.J., Grosse-Kunstleve, R.W., Adams, P.D., Winn, M.D., Storoni, L.C. and Read, R.J. (2007) Phaser crystallographic software. *J Appl Crystallogr*, **40**, 658-674.
32. Afonine, P.V., Grosse-Kunstleve, R.W., Echols, N., Headd, J.J., Moriarty, N.W., Mustyakimov, M., Terwilliger, T.C., Urzhumtsev, A., Zwart, P.H. and Adams, P.D. (2012) Towards automated crystallographic structure refinement with phenix.refine. *Acta Crystallogr D Biol Crystallogr*, **68**, 352-367.
33. Emsley, P. and Cowtan, K. (2004) Coot: model-building tools for molecular graphics. *Acta Crystallogr D Biol Crystallogr*, **60**, 2126-2132.
34. DeLano, W.L. (2009). Nature Publishing Group, a division of Macmillan Publishers Limited. All Rights Reserved.
35. Sigrist, C.J., Cerutti, L., de Castro, E., Langendijk-Genevaux, P.S., Bulliard, V., Bairoch, A. and Hulo, N. (2010) PROSITE, a protein domain database for functional characterization and annotation. *Nucleic Acids Res*, **38**, D161-166.
36. Holm, L. and Rosenstrom, P. (2010) Dali server: conservation mapping in 3D. *Nucleic Acids Res*, **38**, W545-549.
37. Thompson, J.D., Higgins, D.G. and Gibson, T.J. (1994) CLUSTAL W: improving the sensitivity of progressive multiple sequence alignment through sequence weighting, position-specific gap penalties and weight matrix choice. *Nucleic Acids Res*, **22**, 4673-4680.
38. Robert, X. and Gouet, P. (2014) Deciphering key features in protein structures with the new ENDscript server. *Nucleic Acids Res*, **42**, W320-324.
39. Goldenberg, O., Erez, E., Nimrod, G. and Ben-Tal, N. (2009) The ConSurf-DB: pre-calculated evolutionary conservation profiles of protein structures. *Nucleic Acids Res*, **37**, D323-327.

40. Baker, N.A., Sept, D., Joseph, S., Holst, M.J. and McCammon, J.A. (2001) Electrostatics of nanosystems: application to microtubules and the ribosome. *Proc Natl Acad Sci U S A*, **98**, 10037-10041.
41. Gercezi, T. and Correll, C.C. (2004) Imp3p and Imp4p mediate formation of essential U3-precursor rRNA (pre-rRNA) duplexes, possibly to recruit the small subunit processome to the pre-rRNA. *Proc Natl Acad Sci U S A*, **101**, 15301-15306.
42. George, R.A. and Heringa, J. (2002) An analysis of protein domain linkers: their classification and role in protein folding. *Protein Eng*, **15**, 871-879.
43. Wootton, J.C. and Drummond, M.H. (1989) The Q-linker: a class of interdomain sequences found in bacterial multidomain regulatory proteins. *Protein Eng*, **2**, 535-543.
44. Durante-Rodriguez, G., Valderrama, J.A., Mancheno, J.M., Rivas, G., Alfonso, C., Arias-Palomo, E., Llorca, O., Garcia, J.L., Diaz, E. and Carmona, M. (2010) Biochemical characterization of the transcriptional regulator BzdR from *Azoarcus* sp. CIB. *J Biol Chem*, **285**, 35694-35705.
45. Shastry, S. and Hancock, W.O. (2010) Neck linker length determines the degree of processivity in kinesin-1 and kinesin-2 motors. *Curr Biol*, **20**, 939-943.
46. Leidig, C., Thoms, M., Holdermann, I., Bradatsch, B., Berninghausen, O., Bange, G., Sinning, I., Hurt, E. and Beckmann, R. (2014) 60S ribosome biogenesis requires rotation of the 5S ribonucleoprotein particle. *Nat Commun*, **5**, 3491.
47. Basu, U., Si, K., Warner, J.R. and Maitra, U. (2001) The *Saccharomyces cerevisiae* TIF6 gene encoding translation initiation factor 6 is required for 60S ribosomal subunit biogenesis. *Mol Cell Biol*, **21**, 1453-1462.
48. Groft, C.M., Beckmann, R., Sali, A. and Burley, S.K. (2000) Crystal structures of ribosome anti-association factor IF6. *Nat Struct Biol*, **7**, 1156-1164.
49. Ceci, M., Gaviraghi, C., Gorrini, C., Sala, L.A., Offenhauser, N., Marchisio, P.C. and Biffo, S. (2003) Release of eIF6 (p27BBP) from the 60S subunit allows 80S ribosome assembly. *Nature*, **426**, 579-584.
50. Shammas, C., Menne, T.F., Hilcenko, C., Michell, S.R., Goyenechea, B., Boocock, G.R., Durie, P.R., Rommens, J.M. and Warren, A.J. (2005) Structural and mutational analysis of the SBDS protein family. Insight into the leukemia-associated Shwachman-Diamond Syndrome. *J Biol Chem*, **280**, 19221-19229.
51. Menne, T.F., Goyenechea, B., Sanchez-Puig, N., Wong, C.C., Tonkin, L.M., Ancliff, P.J., Brost, R.L., Costanzo, M., Boone, C. and Warren, A.J. (2007) The Shwachman-Bodian-Diamond syndrome protein mediates translational activation of ribosomes in yeast. *Nat Genet*, **39**, 486-495.
52. Finch, A.J., Hilcenko, C., Basse, N., Drynan, L.F., Goyenechea, B., Menne, T.F., Gonzalez Fernandez, A., Simpson, P., D'Santos, C.S., Arends, M.J. *et al.* (2011) Uncoupling of GTP hydrolysis from eIF6 release on the ribosome causes Shwachman-Diamond syndrome. *Genes Dev*, **25**, 917-929.
53. Hall, G.W., Dale, P. and Dodge, J.A. (2006) Shwachman-Diamond syndrome: UK perspective. *Arch Dis Child*, **91**, 521-524.
54. Horiguchi, G., Kodama, H. and Iba, K. (2003) Mutations in a gene for plastid ribosomal protein S6-like protein reveal a novel developmental process required for the correct organization of lateral root meristem in *Arabidopsis*. *Plant J*, **33**, 521-529.
55. de Oliveira, J.F., Sforca, M.L., Blumenschein, T.M., Goldfeder, M.B., Guimaraes, B.G., Oliveira, C.C., Zanchin, N.I. and Zeri, A.C. (2010) Structure, dynamics, and RNA interaction analysis of the human SBDS protein. *J Mol Biol*, **396**, 1053-1069.
56. Graindorge, J.S., Rousselle, J.C., Senger, B., Lenormand, P., Namane, A., Lacroute, F. and Fasiolo, F. (2005) Deletion of EFL1 results in heterogeneity of the 60 S GTPase-associated rRNA conformation. *J Mol Biol*, **352**, 355-369.
57. Jorgensen, R., Ortiz, P.A., Carr-Schmid, A., Nissen, P., Kinzy, T.G. and Andersen, G.R. (2003) Two crystal structures demonstrate large conformational changes in the eukaryotic ribosomal translocase. *Nat Struct Biol*, **10**, 379-385.

58. Klinge, S., Voigts-Hoffmann, F., Leibundgut, M., Arpagaus, S. and Ban, N. (2011) Crystal structure of the eukaryotic 60S ribosomal subunit in complex with initiation factor 6. *Science*, **334**, 941-948.
59. Spahn, C.M., Gomez-Lorenzo, M.G., Grassucci, R.A., Jorgensen, R., Andersen, G.R., Beckmann, R., Penczek, P.A., Ballesta, J.P. and Frank, J. (2004) Domain movements of elongation factor eEF2 and the eukaryotic 80S ribosome facilitate tRNA translocation. *EMBO J*, **23**, 1008-1019.
60. Gartmann, M., Blau, M., Armache, J.P., Mielke, T., Topf, M. and Beckmann, R. (2010) Mechanism of eIF6-mediated inhibition of ribosomal subunit joining. *J Biol Chem*, **285**, 14848-14851.
61. Gijssbers, A., Garcia-Marquez, A., Luviano, A. and Sanchez-Puig, N. (2013) Guanine nucleotide exchange in the ribosomal GTPase EFL1 is modulated by the protein mutated in the Shwachman-Diamond Syndrome. *Biochem Biophys Res Commun*, **437**, 349-354.
62. Taylor, D.J., Nilsson, J., Merrill, A.R., Andersen, G.R., Nissen, P. and Frank, J. (2007) Structures of modified eEF2 80S ribosome complexes reveal the role of GTP hydrolysis in translocation. *EMBO J*, **26**, 2421-2431.
63. Gai, Z., Kitagawa, Y., Tanaka, Y., Shimizu, N., Komoda, K., Tanaka, I. and Yao, M. (2012) The binding mechanism of eIF2beta with its partner proteins, eIF5 and eIF2Bepsilon. *Biochem Biophys Res Commun*, **423**, 515-519.

Acknowledgements

The thesis is result of almost five years of work, and it would be impossible to accomplish this work without many people who supported me and believed in me.

First of all I would like to acknowledge the enthusiastic supervision Professor Yao Min for giving opportunity to be involved in various research projects. Her many advises and encouraging my research allow me to grow as a research scientist.

I would also like to give my thanks to Professor Isao Tanaka for his guidance, suggestion and discussion on all stages of my research. The discussions with him broaden my horizons, and his suggestions lead me to get doctoral degree.

I would also be grateful for Associated Professor Yoshikazu Tanaka for his suggestion and discussion. His focus points always impress me.

I thank Ms. Yoshie Kudo, the secretary of Yao's Lab, for her valuable support. I also thank Dr. Koji Kato for his kind advice and discussion especially for structure analysis, Dr. Keisuke Komoda for his kind advice and encouragement, Dr. Akiyoshi Nakamura for his guidance of various experiments and critical discussion from my 3rd grade, Dr. Akira Shinoda for his kind advice, discussion and phase determination. Thanks to all member of Yao's Lab. For a good cooperation and happy life.

Finally, I thank my parents very much for their support and courage.

Thank you everyone.